Article

Cell Chemical Biology

# 1-deoxysphingolipids dysregulate membrane properties and cargo trafficking in the early secretory pathway

## Graphical abstract

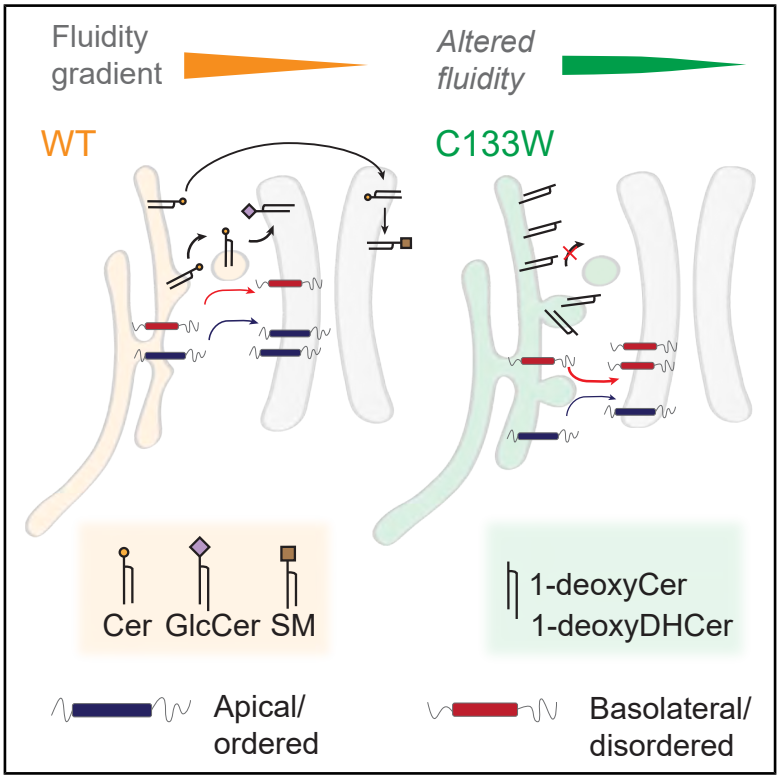


## Highlights

- Bioorthogonal labeling of 1-deoxysphingolipids reveals their retention in the ER
- Mutant serine palmitoyl transferases drive 1-deoxysphingolipid synthesis
- Accumulation of 1-deoxysphingolipids causes a loss of ER membrane properties
- 1-deoxysphingolipids modulate membrane protein cargo release from the ER

## Authors

Yi-Ting Tsai, Nicolas-Frédéric Lipp, Olivia Seidel, ..., Sonya Neal, Christian M. Metallo, Itay Budin

## Correspondence

ibudin@ucsd.edu

## In brief

Tsai et al. show that a class of atypical sphingolipids, 1-deoxysphingolipids, is retained in endoplasmic reticulum membranes, where they alter lipid packing and change the kinetics of membrane protein secretion rates. These effects could be relevant for human diseases in which 1-deoxysphingolipids accumulate in cells.

Tsai et al., 2026, Cell Chemical Biology *33*, 45–58
January 15, 2026 
https://doi.org/10.1016/j.chembiol.2025.12.006

CellPress

Cell Chemical Biology

CellPress
OPEN ACCESS

Article

# 1-deoxysphingolipids dysregulate membrane properties and cargo trafficking in the early secretory pathway

Yi-Ting Tsai,[1] Nicolas-Frédéric Lipp,[1,7] Olivia Seidel,[1,7] Riya Varma,[1] Aurelie Laguerre,[2,3] Kristina Solorio-Kirpichyan,[4] Adrian M. Wong,[1] Roberto J. Brea,[1,5] Grace H. McGregor,[2,3] Thekla Cordes,[2,3] Neal K. Devaraj,[1] Lars Kuerschner,[6] Sonya Neal,[4] Christian M. Metallo,[2,3] and Itay Budin[1,8,*]

[1]Department of Biochemistry & Molecular Biophysics, University of California, San Diego, La Jolla, CA 92093, USA
[2]Department of Bioengineering, University of California, San Diego, La Jolla, CA 92093, USA
[3]Salk Institute of Biological Studies, La Jolla, CA 92037, USA
[4]Department of Cell and Developmental Biology, University of California, San Diego, La Jolla, CA 92093, USA
[5]CICA - Centro Interdisciplinar de Química e Bioloxía e Departamento de Química, Facultade de Ciencias, Universidade da Coruña, Rúa As Carballeiras, 15701 A Coruña, Spain
[6]Life & Medical Sciences Institute, University of Bonn, 53115 Bonn, Germany
[7]These authors contributed equally
[8]Lead contact
*Correspondence: ibudin@ucsd.edu
https://doi.org/10.1016/j.chembiol.2025.12.006

**SIGNIFICANCE** Sphingolipid metabolism begins with the condensation of the amino acid L-serine with palmitoyl-CoA by serine palmitoyl-CoA transferase (SPT), an enzyme residing in the endoplasmic reticulum (ER). Changes to amino acid levels or the expression of specific SPT alleles can drive the misincorporation of L-alanine in place of L-serine, leading to the formation of sphingolipids lacking the C1 hydroxyl group. These 1-deoxysphingolipids (1-deoxySLs) are linked to several genetic and metabolic disorders, including type II diabetes, hereditary sensory and autonomic neuropathy type 1, and macular telangiectasia (MacTel). In patients with MacTel, retinal pigment epithelium (RPE) cells exhibit a loss of displayed phagocytic receptors, suggesting a potential role for 1-deoxySLs in the trafficking of membrane proteins. Motivated by this observation, we investigated the distribution and functions of 1-deoxySLs in secretory membranes. First, we applied metabolic labeling and organelle-targeted biorthogonal reactions to visualize 1-deoxySLs in early secretory compartments, finding that they become enriched in the ER and at ER exit sites (ERESs) in an RPE cell line. Second, we expressed disease-causing SPT variants to drive the accumulation of 1-deoxySLs and investigated their effects on ER structure and function. We found that these lipids do not induce classic ER stress pathways but instead reduce membrane fluidity in the compartment and alter the ERES. Using synchronized protein release experiments, we showed that these changes correlated with either increased ER retention of membrane proteins that are typically found on the apical membranes of polarized RPE. In contrast, membrane proteins that are trafficked to basolateral membranes are released faster from the ER. These results suggest that 1-deoxySL accumulation might modulate membrane protein trafficking through the secretory pathway, which could drive cell type-specific responses in 1-deoxySL-associated diseases.

## SUMMARY

1-Deoxysphingolipids are non-canonical sphingolipids linked to several diseases, yet their cellular effects are poorly understood. Here, we utilize lipid chemical biology approaches to investigate the role of 1-deoxysphingolipid metabolism on the properties and functions of secretory membranes. We applied organelle-specific bioorthogonal labeling to visualize the subcellular distribution of metabolically tagged sphingolipids. We observed that 1-deoxysphingolipids are retained in the endoplasmic reticulum (ER) and specifically in ER exit sites (ERESs), suggesting that they do not efficiently sort into vesicular carriers. Cell lines expressing disease-associated variants of serine palmitoyl-CoA transferase accumulated

1-deoxysphingolipids, which were accompanied by a reduction in ER membrane fluidity and enlargement of ERES. We found that the rates of membrane protein release from the ER were altered in response to 1-deoxysphingolipid metabolism in a manner dependent on the protein's affinity for ordered or disordered membranes. The dysregulation of sphingolipid metabolism can thus alter secretory membrane properties and affect protein trafficking.

## INTRODUCTION

Sphingolipids (SLs) represent a major class of cell membrane and signaling lipids whose dysregulation is associated with a range of metabolic diseases. SL biosynthesis is initiated by the condensation of L-serine with fatty acyl-CoAs by serine palmitoyl-CoA transferase (SPT), a heteromeric ER membrane protein complex consisting of both catalytic and regulatory subunits.[1] The ketosphinganine product of SPT is rapidly reduced to sphinganine (SA), the building block of all SLs (Figure 1A). From its L-serine precursor, the sphingoid base of SA retains a secondary amine, which is *N*-acylated to form dihydroceramides (DHCers) that are *trans* desaturated at the 4,5 position into ceramides (Cers), and a primary hydroxyl group at the C1 position, which is modified by polar groups at the Golgi apparatus[2] to form the complex SLs sphingomyelin (SM) and glycosphingolipids (glycoSLs), such as glucosyl ceramide (GlcCer), galactosyl ceramide (GalCer), lactosyl ceramides (LactosylCer), and gangliosides. Complex SLs are enriched in the exoplasmic/luminal leaflet of late secretory vesicles and contribute substantially to the ordered nature of these bilayers.[3]

SPT can also incorporate alternative amino acids in place of L-serine, most commonly L-alanine. The resulting products – 1-deoxy ketosphinganine and 1-deoxy sphinganine (deoxySA) – lack the C1 hydroxyl on the sphingoid base. They are *N*-acylated to form 1-deoxydihydroceramide (deoxyDHCer), which is desaturated into 1-deoxyceramide (deoxyCer), although the resulting double bond is likely *cis* and positioned further down the sphingoid chain than the Cer.[4] Unlike canonical SLs, dihydro species accumulate in the 1-deoxy pathway, reflecting C1 hydroxyl substrate specificity for dihydroceramide desaturase (DEGS1). These 1-deoxysphingolipids (1-deoxySLs) also cannot be further modified into complex SLs, such as sphingomyelin (SM) or glycosphingolipids (glycoSL), nor broken down by the canonical SL degradation pathway,[5] both of which require modifications on the C1 hydroxyl group. They thus represent an alternative branch of SL biosynthesis.[6] 1-DeoxySLs, especially the dihydro species (deoxDHCer) that are abundant in cells, retain the high melting temperature of Cers but are even less miscible due to their extreme hydrophobicities.[7,8]

While first identified in mollusks[9] and pathogenic fungi,[10] 1-deoxySLs have more recently been recognized as endogenous metabolites in mammalian cells, and as potential drivers of human disease.[11] In mammals, 1-deoxySL metabolism is controlled by amino acid concentrations and the substrate selectivity of SPT. Depletion of serum L-serine levels causes accumulation in patients with type 2 diabetes mellitus (T2DB), for which 1-deoxySLs serve as a biomarkers[12] and may function in associated diabetic sensory polyneuropathy (DSN).[13] Specific alleles of SPT subunits that lose substrate selectivity for L-serine can also drive disease metabolism. Mutations in the SPT catalytic subunits *SPTLC1* or *SPTLC2* are causative for hereditary sensory and autonomic neuropathy type 1 (HSAN1), an axonal neuropathy whose severity is correlated with plasma 1-deoxySL levels.[14] When expressed in cells, HSAN1-associated alleles of SPT subunits cause large increases in substrate affinity for L-alanine vs. L-serine.[15] The expression of *SPTLC1* disease-associated variants was shown to drive pathologies in animal models,[16] which are rescued by the heterozygous overexpression of WT alleles.[17] Patients with HSAN1 also show high susceptibility to develop macular telangiectasia type 2 (MacTel),[18] which manifests in adult-onset blindness and correlates with low serum L-serine levels.[19] In patients with MacTel, the macula features distinct regions of pigment loss, while the subretinal space between photoreceptors and the Retinal Pigment Epithelium (RPE) accumulates rod outer segments (ROS) and other cell debris.[20] Such subretinal deposits are also signatures of other forms of macular degeneration.[21] MacTel patient RPE cells show reduced cell surface expression of MerTK,[22] an apical membrane receptor for phagocytic recycling of ROS,[23] suggesting a potential mechanism for the accumulation of subretinal debris.

Mechanisms underlying 1-deoxySL toxicity in cells or tissue-specific phenotypes in patients are still unresolved. Phenotypic effects of 1-deoxySLs are often assayed in cell culture by medium supplementation with exogenous 1-deoxySA, comparing its effects with equivalent concentrations of SA. After uptake, 1-deoxySA is converted into the corresponding 1-deoxyDHCer and 1-deoxyCers that localize to a range of cellular compartments, including mitochondria, Golgi, and lysosomes, as imaged by bioorthogonal reactive handles.[24] Resulting toxicities vary by cell type, with cancer cells[25] and neurons[26] being particularly sensitive. Reported molecular phenotypes upon supplementation with μM-concentrations of 1-deoxySA include the induction of the unfolded protein response (UPR),[27] pro-apoptotic PKC signaling,[25,28] autophagosome formation,[29] and loss of mitochondrial respiration.[5] Supplementation of 1-deoxySA depends on cell permeability for single-chain SLs, which are expected to diffuse between intracellular membranes.[30] In contrast, endogenous SA is produced in the ER and then metabolized to insoluble double-chained SL products, all of which must be trafficked by lipid transport pathways. 1-DeoxySL accumulation is higher in typical 1-deoxySA supplementation experiments than from the expression of disease-associated SPT variants.[31] Thus, it is not clear if exogenously added SL metabolites fully reflect the localization and phenotypes of those that are endogenously produced. An alternative approach to investigating 1-deoxySL function is the study of patient-derived cell lines with SPT mutations[32] or heterologous expression of these SPT variants in engineered cell lines.[31]

Here, we apply a combination of chemical and cell biology approaches to investigate the role of 1-deoxySLs in the secretory

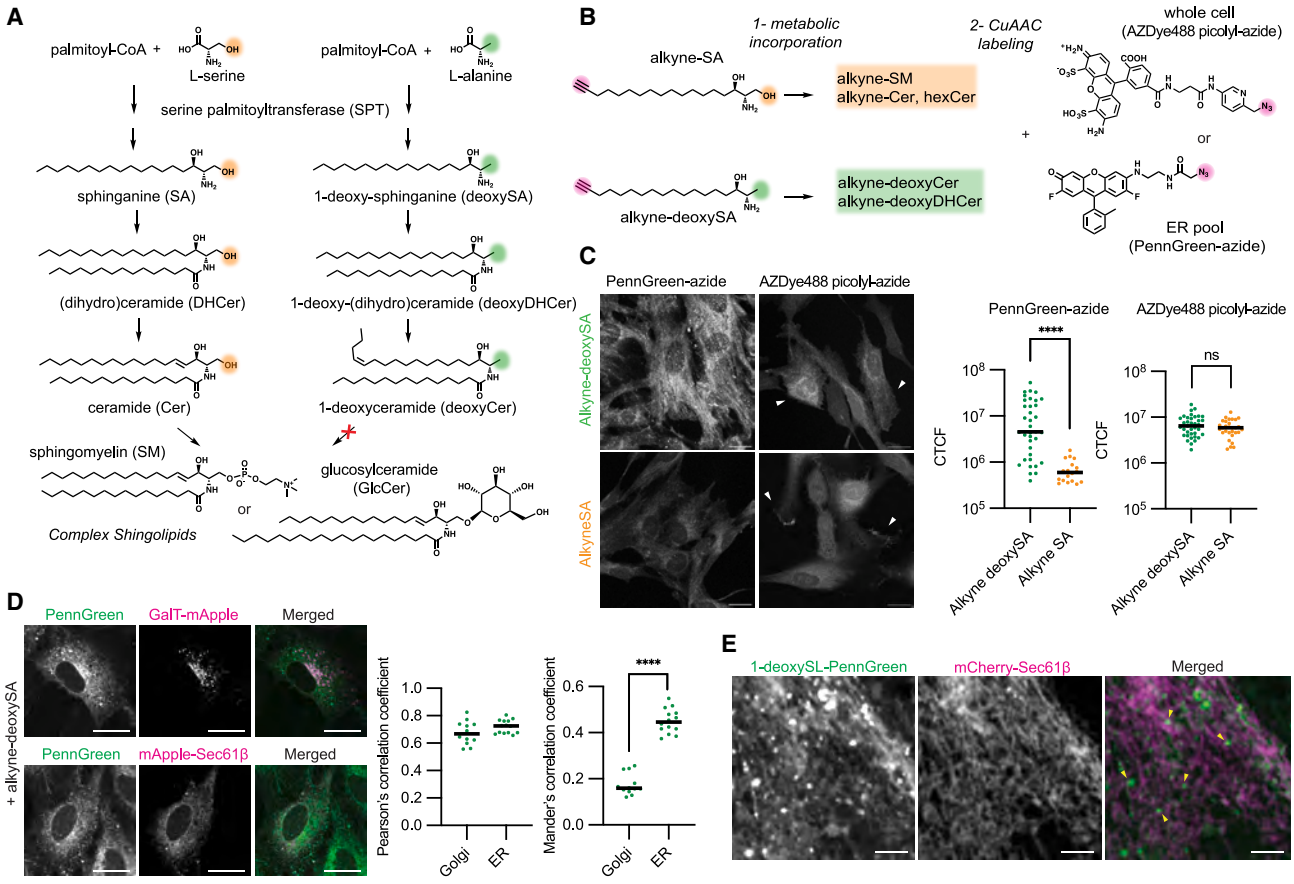


**Figure 1. Organelle-specific labeling of 1-deoxySLs identifies their accumulation in early secretory membranes**

(A) SL and 1-deoxySL biosynthetic pathway depicting the intermediate lipid species and their chemical structures.

(B) The approach utilized in this study to identify the localization of 1-deoxySL in subcellular compartments. RPE-1 cells were fed either with 0.1 μM alkyne-deoxySA or 0.1 μM alkyne-SA for 17 h, after which cells were fixed and the CuAAC reaction was carried out with either PennGreen-azide or AZDye488 picolyl-azide.

(C) Imaging of RPE-1 cells fed with either alkyne-deoxySA or alkyne-SA and reacted with PennGreen-azide or AZDye488 picolyl-azide. Scale bars, 20 μm. Alkyne-deoxySA treatment led to a larger PennGreen-azide level than for alkyne-SA. Each point represents an individual field of cells across two biological replicates. ****, $p < 0.0001$ by Mann-Whitney test. AZDye488 picolyl-azide labeling instead showed in localization: the alkyne-deoxySA showed a distinct ER localization, while alkyne-SA was observed at PM ruffles (arrows).

(D) Colocalization of 1-deoxySL-PennGreen products with Golgi (GalT-mApple) and ER (mApple-Sec61β) markers. Representative images are shown to the left and quantification of the Pearson's and Mander's correlation coefficients to the right. PennGreen is correlated with both markers but overlaps more with the ER. Each point represents an individual cell. ****, $p < 0.0001$ by Mann-Whitney test. Scale bars, 20 μm.

(E) Airyscan images show that the co-localization of 1-deoxySL-PennGreen products with mCherry-Sec61β, with additional puncta dispersed through the network, is indicated by the arrows in the merged image. Scale bars, 2.5 μm.

pathway of cells. We were motivated by the reduced surface display of membrane proteins in the RPE of patients with MacTel to consider the role of 1-deoxySLs metabolism in secretory pathway function. Utilizing an immortalized RPE cell line as a model, we report that 1-deoxySLs accumulate in the early secretory pathway, where they alter ER membrane fluidity and protein cargo export.

## RESULTS

### 1-deoxysphingolipids accumulate in the early secretory pathway

The most abundant 1-deoxySLs, deoxyCers, and deoxyDHCers are synthesized in the ER alongside their corresponding SL precursors. Cers are efficiently exported from the ER membrane by both vesicular and non-vesicular pathways,[2] and we asked if this was the case for their 1-deoxy counterparts. Bioorthogonal chemistry is one approach to image subcellular distributions of specific membrane lipids, provided that tracers can be fed to cells that can be readily incorporated into native metabolic pathways and feature minimally disruptive chemical handles.[33] The single-chain SL precursor SA modified with a terminal alkyne (alkyne-SA), alongside its 1-deoxy counterpart (alkyne-deoxySA) (Figure 1B), can be used to visualize SL distributions through copper(I)-catalyzed alkyne-azide cycloaddition (CuAAC) with azide-containing fluorophores.[5] Previous analyses with alkyne-deoxySA fed cells showed its incorporation into deoxyDHCer and deoxyCer species and staining of several

compartments within cells, including the ER, Golgi, mitochondria, and lysosomes.[5,29]

To better visualize the distribution of 1-deoxySLs at their site of synthesis and transport in the early secretory pathway, we sought to employ organelle-targeted bioorthogonal chemistry. The fluorophore Pennsylvania localizes predominantly to ER and Golgi membranes through its rhodol group[34] and can specifically label azido-labeled lipids[35] and native proteins[36] in these compartments. To carry out such an analysis, we synthesized an azido Pennsylvia Green (PennGreen-azide) that is compatible with CuAAC reactions (STAR Methods). We confirmed that PennGreen-azide localized predominantly to ER and Golgi membranes, with some residual staining of mitochondria as previously observed (Figure S1A). Cells were incubated with trace amounts of alkyne-SA and alkyne-deoxySA (0.1 μM) before PennGreen-azide labeling. Cells not treated with an alkyne lipid showed no residual PennGreen signal after washing steps (Figure S1B).

We contrasted labeling patterns after CuAAC reactions with PennGreen-azide with those utilizing AZDye488 picolyl azide, a non-targeted fluorophore that reacts with buried alkynes in membranes.[37] Canonical SL products, labeled with alkyne-SA, showed robust staining with AZDye488 picolyl-azide, but low labeling with PennGreen-azide (Figure 1C), consistent with their rapid transport from the ER and Golgi to later secretory compartments where they accumulate. In contrast, 1-deoxySLs, labeled with alkyne-deoxySA, showed a strong signal when labeled with PennGreen-azide. In AZDye488 picolyl-azide experiments, labeling distributions were also different for each probe: cells fed with alkyne-SA showed staining at the PM, while those with alkyne-deoxySA were retained in the ER (Figure 1C, arrows). In alkyne-deoxySA fed cells, the signal for the PennGreen product (PennGreen-1-deoxySL) was correlated with that of both ER (Sec61β) and Golgi (GalT) markers but predominantly overlapped with the former (Figure 1D). These data were broadly consistent with experiments showing that 1-deoxy variants of C6-NBD-Ceramide are retained in the ER.[38] High-resolution Airyscan micrographs showed that PennGreen-1-deoxySL signal colocalized with the peripheral ER network but also accumulated at dispersed puncta that were not labeled with Sec61β (Figure 1D).

## 1-deoxysphingolipid accumulation occurs at sites of vesicular trafficking

We next considered the mechanism by which 1-deoxySLs become retained in the ER. Canonical ceramides are trafficked from the ER through vesicular and non-vesicular mechanisms (Figure 2A). The lipid transfer protein (LTP) CERT[39] localizes to ER-Golgi contact sites[40] and contributes to SM synthesis by Golgi-localized SMS1.[41] The structure of CERT bound to ceramide ligands shows hydrogen bonding interactions between residues in the (StAR)-related lipid transfer (START) domain and the C1-hydroxyl of ceramide, which is absent in 1-deoxySLs (Figure 2B). To test whether the absence of this interaction alters CERT activity, we synthesized a 1-deoxyDHCer with a C12-NBD *N*-acyl chain and a version containing the C1-hydroxyl group for use in FRET-based lipid transfer assays. Addition of purified CERT START domain initiated dequenching of the NBD lipids as they were transferred into liposomes lacking the FRET acceptor Rhodamine-PE (Figure 2C). We measured that the initial transfer rate for CERT acting on C12-NBD-deoxyDHCer was ~2-fold higher than that of C12-NBD-DHCer (Figure 2D). Transport (Figure 2E) for both was slowed by the competitive inhibitor HPA-12, indicating that they are trafficked via the same binding pocket. The increased transfer rate upon loss of ligand affinity has been observed for other lipid transporters.[42]

CERT-independent pathway(s) of ceramide trafficking are responsible for glucosylceramide synthesis,[43] and are thought to involve vesicular carriers at ER exit sites (ERESs).[44] Sorting and trafficking of lipids to ERES is presumed to rely on their partitioning in the ER network.[45] If this segregation is impeded by the reduced solubility and increased hydrophobicity of 1-deoxySLs, we hypothesized that they would accumulate proximal to ERES. The 1-deoxySL-PennGreen puncta we previously observed dispersed through the ER network (Figure 1E) co-localized with the COP-II marker mCherry-Sec23, indicating accumulation at or near ERES (Figure 2F). High-resolution imaging revealed a randomly oriented offset of 100–200 nm between mCherry-Sec23 and 1-deoxySL-PennGreen (Figure 2G), the approximate size of ERES across a range of cell types.[45] 1-deoxySLs thus accumulate at regions within or proximal to ERES, which could reflect increased flux through vesicular trafficking, reduced sorting of 1-deoxySLs from exit sites to carriers, or inhibition of vesicular carrier release.

## A disease-associated serine palmitoyl-CoA transferase variant recapitulates 1-deoxysphingolipids overproduction

Cers and 1-deoxyCers show a propensity to form high order gel-like membrane domains due to their immiscibility with other lipids *in vitro,*[8] which is even stronger for 1-deoxyDH species.[7] If 1-deoxySLs accumulate in the ER, we hypothesized that their overproduction would drive changes to ER structure and function. To promote 1-deoxySL synthesis without altering amino acid availability, which directly induces ER stress,[46,47] we constructed stable cell lines in which 1-deoxySL synthesis is induced through the doxycycline-inducible expression of the C133W allele of *SPTLC1* ($SPT^{C133W}$), the most common mutation identified in patients with HSAN1.[48] To control for overexpression effects, we generated an analogous strain harboring the wild-type (WT) variant of *SPTLC1* ($SPT^{WT}$) which showed similar expression upon induction (Figure 3A). In the absence of doxycycline, the growth of both $SPT^{WT}$ and $SPT^{C133W}$ was identical to RPE-1. Only the latter showed a growth defect under induction maximum conditions (Figure 3B). Thus, SPT overexpression itself is not deleterious to RPE-1 cells under these growth conditions.

Lipidomics analyses for induced $SPT^{C133W}$ cells showed a 4 and 10-fold increase in deoxyCers and deoxyDHCers, respectively, over uninduced $SPT^{C133W}$ cells (Figures 3C and S2A) and the induced $SPT^{WT}$ control strain (Figures 3D and S2B). Induced $SPT^{WT}$ and $SPT^{C133W}$ showed identical Cer and complex SLs, except for a minor increase in SM levels in the latter. In contrast, $SPT^{C133W}$ induction led to moderate decreases in Cers, LactosylCer, and SM (Figure 3C). We thus chose the comparison of induced $SPT^{WT}$ and $SPT^{C133W}$, which have similar SL profiles but different 1-deoxySL levels, for follow up experiments.

In addition to the expression of SPT mutants, 1-deoxySLs can also accumulate in response to changes in the L-alanine (Ala) to

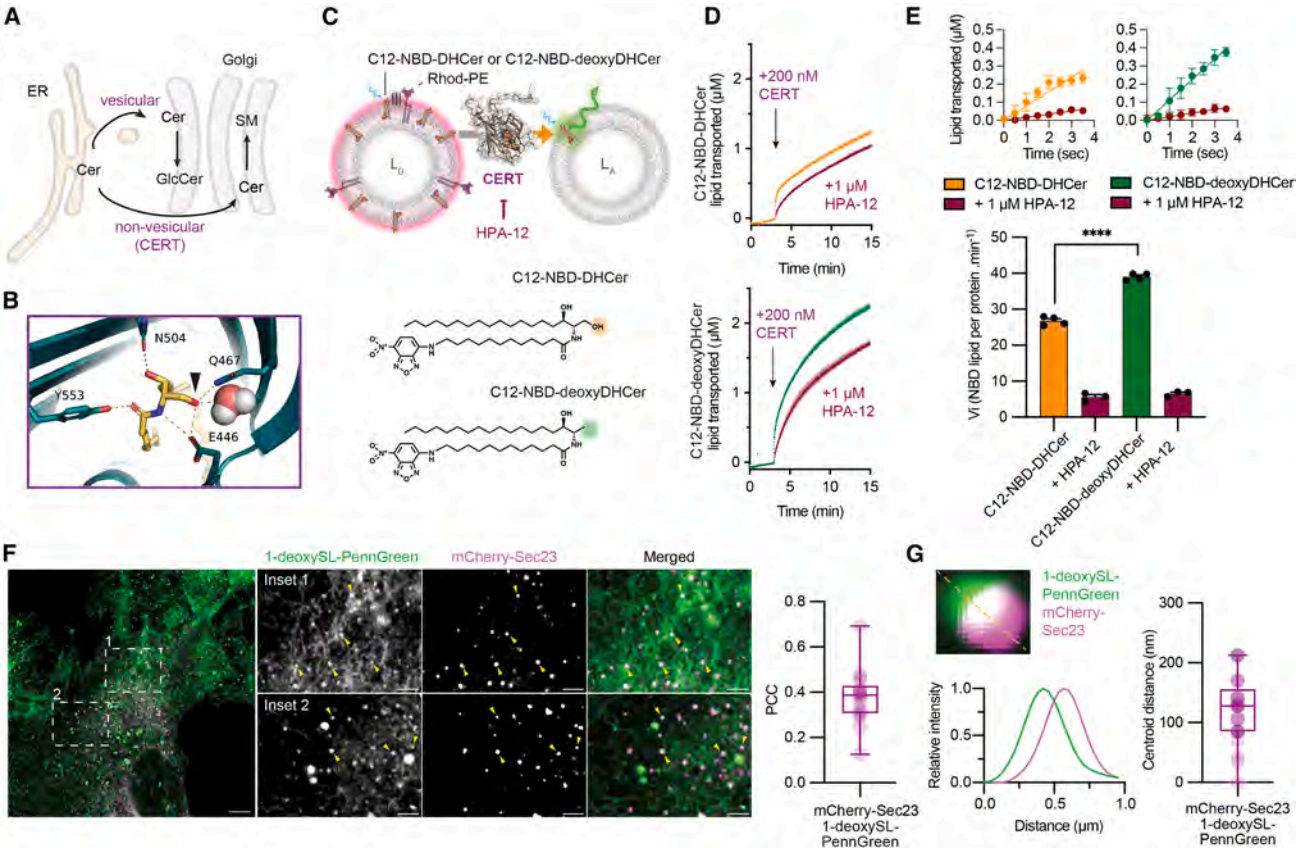


**Figure 2. 1-DeoxySLs are transported by CERT but accumulate at sites of vesicular trafficking**

(A) Cer produced in the ER can be exported to the Golgi via vesicular or non-vesicular trafficking, the latter is mediated by the CERT.

(B) CERT's START domain makes polar contacts with the C1 hydroxyl of Cer (PDB: 2E3O).

(C) Measurements of CERT transport using FRET-based assay (top) and the structure of C12-NBD-DHCer/C12-NBD-deoxyDHCer (bottom). Donor liposomes ($L_D$) contained 93(mol)% di-oleoyl-phosphatidylcholine (DOPC), 5% of the NBD-labeled lipid, and 2% rhodamine-phosphatidylethanolamine (Rhod-PE). Acceptor liposomes ($L_A$) contained only DOPC.

(D) Lipid transport curves for C12-NBD-DHCer (top) or C12-NBD-deoxyDHCer (bottom) upon the injection of CERT. CERT transports C12-NBD-deoxyDHCer faster than C12-NBD-DHCer, and transport of both is slowed in the presence of 1 μM of the competitive inhibitor HPA-12.

(E) Initial transport rates calculated over the first transport phase. Linear fits are shown above, while calculated rates are plotted later in discussion. For rates, error bars show SEM ($N = 4$ independent experiments per condition). ****, $p < 0.0001$ by an unpaired Welch's $t$ test.

(F) RPE-1 cells incubated with 0.1 μM 1-deoxySA and labeled with PennGreen-azide, as in Figure 1. 1-DeoxySL-PennGreen products are observed at puncta that co-localize with mCherry-Sec23. The Pearson's correlation coefficient (PCC) between 1-deoxySL-PennGreen and mCherry-Sec23 is shown for 17 cells.

(G) The centroid of 1-deoxySL-PennGreen puncta overlaps with those of mCherry-Sec23 but shows an average offset distance of 120 nm. An example of such overlap is shown with the corresponding two-channel intensity profile. Centroid-to-centroid distances for discrete 29 exit sites chosen from 5 individual cells are provided.

L-serine ratio in the medium, mimicking the effect of amino acid dysregulation observed in metabolic disease.[49] In RPE-1, medium supplementation with 1 mM Ala caused accumulation of deoxyCers and deoxyDHCers compared to control RPE-1 (Figures 3E and S2C). However, deoxyCers and deoxyDHCers levels in Ala-fed RPE-1 were 2- to 3-fold less than those for induced $SPT^{C133W}$, suggesting that mutations in *SPTLC1* can have a larger effect than amino acid concentrations in determining cellular 1-deoxySL levels. In both induced $SPT^{C133W}$ and Ala-supplemented cells, the most abundant 1-deoxySL species were saturated species with 24:0 *N*-acyl chains, e.g., m18:0/24:0 deoxyDHCer, with other very long chain fatty acid (VLCFA) *N*-acyl chains such as 24:1 and 26:0 also abundant (Figure S2). This distribution of acyl chains more closely resembled that of glycoSLs, which are also enriched in VLCFAs, than that of SM or canonical Cers, which have shorter *N*-acyl chains (e.g., C16:0) (Figure 3F).

Exogenously added 1-deoxySAs at μM concentrations causes mitochondrial[24] and ER stress,[27] so we tested whether endogenous 1-deoxySL overproduction causes similar phenotypes. We measured the induction of ER stress through the UPR: phosphorylated forms of the sensors IRE-1 and Akt, and the ER-associated degradation proteins Derlin-1 and Derlin-3. We did not observe changes in the abundance of these markers when comparing uninduced and induced $SPT^{C133W}$ and $SPT^{WT}$ cells (Figure S3A). We also observed that neither $SPT^{C133W}$ nor $SPT^{WT}$ cells showed a reduction in respiratory capacity, indicating a lack of significant mitochondrial

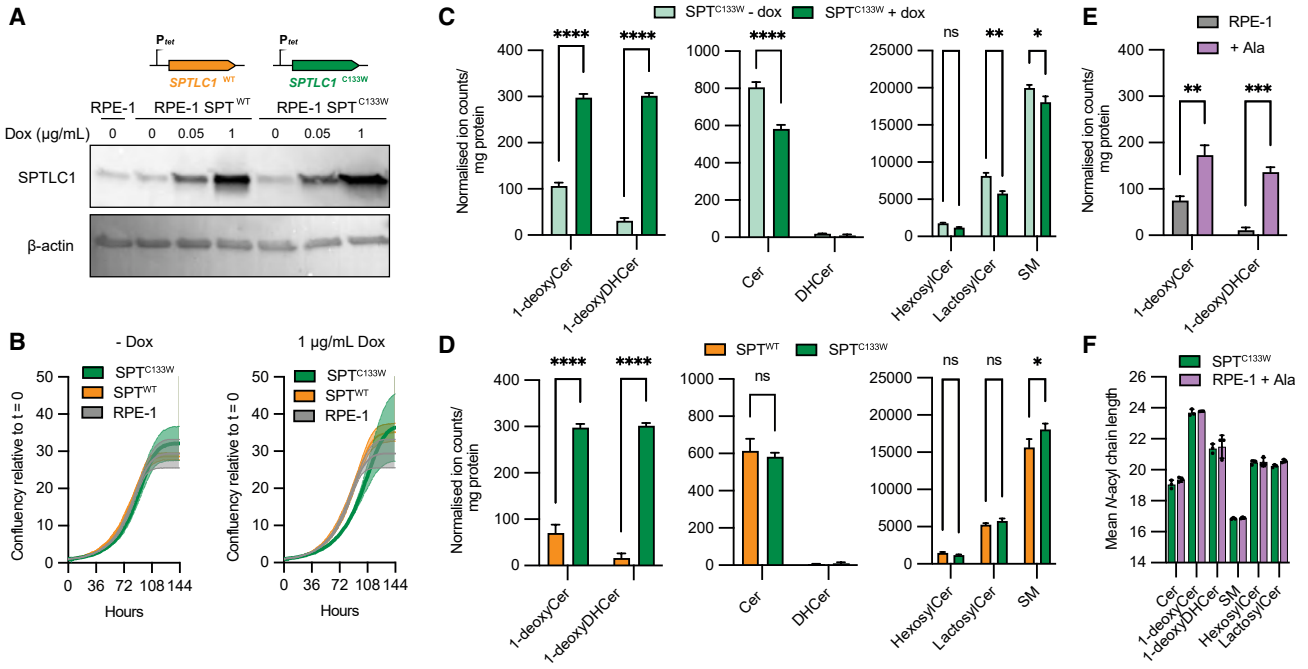


**Figure 3. Endogenous overproduction of 1-deoxySLs in RPE-1**

(A) Immunoblotting of SPTLC-1 in RPE-1 cell line expressing additional copies of wild type ($SPT^{WT}$, orange) or mutant *SPTLC1* ($SPT^{C133W}$, green). Upon incubation with the indicated concentration of doxycycline for 48 h, $SPT^{WT}$ and $SPT^{C133W}$ cell lines show similar SPTLC1 levels. A separate blot for β-actin from the same samples is provided as a loading control.

(B) Growth of RPE-1, $SPT^{WT}$, and $SPT^{C133W}$ is identical under no induction, while the latter shows a modest growth defect under induction. Error bars indicate SEM for $N = 3$ independent wells measured with an IncuCyte system.

(C) Induction of $SPT^{C133W}$ causes high accumulation of 1-deoxy products (left) and depletions of canonical Cers (middle) and complex SLs (right). Levels of SLs and deoxySLs were compared between $SPT^{C133W}$ cells cultured with or without doxycycline.

(D) Compared to induced $SPT^{WT}$ cells, $SPT^{C133W}$ cells show high accumulation of 1-deoxySLs (left) and only small changes to canonical Cers (middle) and complex SLs (right).

(E) Moderate accumulation of 1-deoxySLs in RPE-1 cells supplemented with 1 mM Ala. Normalized ion counts are comparable between panels C-F.

(F) In both $SPT^{C133W}$ and Ala-fed RPE-1 cells, 1-deoxyCer and 1-deoxyDHCer species have an average *N*-acyl chain length (23 carbons) that is longer than canonical Cers (19 carbons). This VLCFA resembles the profile of Hexosyl- and LactosylCers (20 carbons), while SM species (17 carbons) show short *N*-acyl chain lengths. Error bars indicate SEM (extracts from $N = 3$ independent culture dishes). *, $p < 0.05$; **$p < 0.01$; ****, $p < 0.0001$ by two-way ANOVA.

dysfunction (Figure S3B). Thus, the accumulation of 1-deoxySLs in $SPT^{C133W}$ expressing RPE-1 cells is not tied to the mitochondrial and ER stresses previously reported.[5,27]

## 1-deoxysphingolipid accumulation causes altered endoplasmic reticulum membrane packing and endoplasmic reticulum exit sites morphology

In unstressed cells, the ER is largely devoid of high-melting temperature lipids, such as cholesterol, due to the rapid trafficking of these components after their synthesis.[50,51] We hypothesized that the retention of long-chain 1-deoxySLs could thus potently alter ER membrane properties. To measure ordering, we used emission shifts of the solvatochromic dye Laurdan. These were quantified by a unit-less Generalized Polarization (GP) ratio based on pixel intensities taken simultaneously at two emission wavelength windows.[52] Since the dye labels all lipid environments in the cell, we used mCherry-Sec61β to auto-mask the ER-specific Laurdan signal ($GP_{ER}$) (Figure 4A).

GP-heatmaps of RPE-1 showed a generally fluid ER membrane, with variable $GP_{ER}$ values averaging 0 (Figure 4B). In contrast, heatmaps of induced $SPT^{C133W}$ cells showed regions of increased ordering, which were also observed in Ala-fed cells (Figure 4C). Mean $GP_{ER}$ was increased upon $SPT^{C133W}$ induction and Ala-feeding compared to their corresponding controls (Figure 4D), indicating a more ordered ER membrane. This corresponded to reduced $GP_{ER}$ variability, since ordered ER membrane regions showed uniformly high GP (Figure 4E). To test if the increase in $GP_{ER}$ was due to defects in ER exit of 1-deoxySLs or their intrinsic properties, we reduced Cer exit from the ER with the CERT inhibitor HPA-12.[53] Laurdan $GP_{ER}$ increased significantly in cells treated with HPA-12, like that for $SPT^{C133W}$ cells (Figure 4F). Thus, the retention of canonical Cers within the ER can mimic the reduction of ER membrane fluidity observed for 1-deoxySL-synthesizing cells.

The continual enrichment of cholesterol and SLs[54] acts to membrane ordering along the secretory pathway to the plasma membrane (PM). We thus extended our analysis of secretory pathway fluidity to Golgi membranes and the PM using additional segmentation markers (Figure S4). As expected, unperturbed RPE-1 cells showed a monotonic increase in Laurdan GP along the secretory pathway from the ER to Golgi to PM

CellPress
OPEN ACCESS

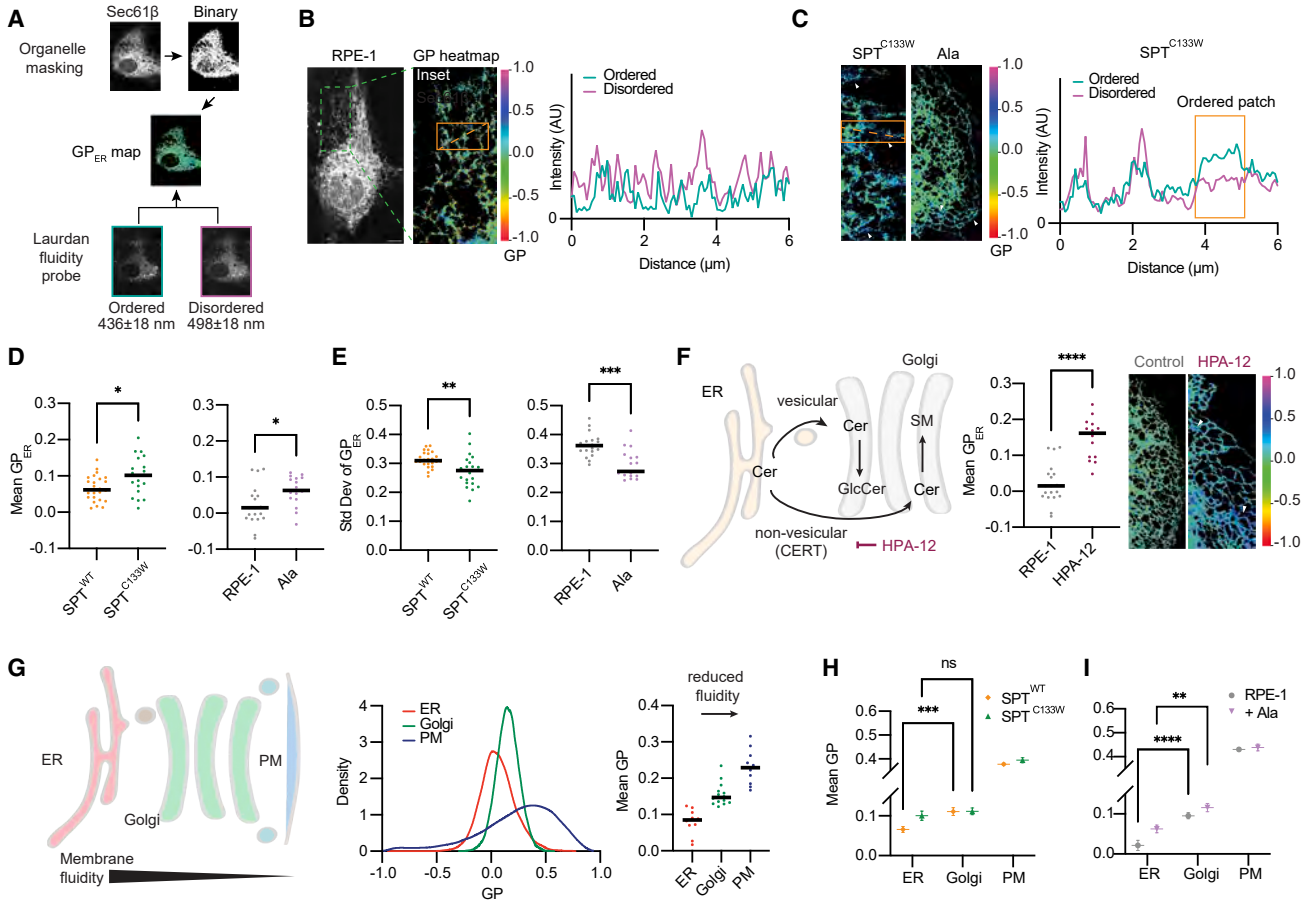


**Figure 4. 1-deoxySL metabolism alters membrane fluidity in the secretory pathway**

(A) Generating ER-localized membrane ordering profiles using segmentation of two-channel confocal fluorescence intensity of Laurdan.

(B) An example of $GP_{ER}$ heatmap for a cell, showing the distribution of the ordered and disordered channel intensities. Scale bars, 10 μm.

(C) Examples for 1-deoxySL-accumulating cells. The profile on the right shows a region of ER in an induced $SPT^{C133W}$ cell with elevated ordered channel signal, reflecting a less fluid membrane.

(D) $GP_{ER}$ for induced $SPT^{C133W}$ cells is higher than that for $SPT^{WT}$ cells. Similarly, Ala-fed RPE-1 cells show increased $GP_{ER}$. Points represent mean $GP_{ER}$ values computed across individual cells ($n$ = 20 ($SPT^{C133W}$), 24 ($SPT^{WT}$), 19 (RPE-1), 17 (Ala)). *, $p < 0.05$ by Mann-Whitney test.

(E) Variability in $GP_{ER}$ within single cells is reduced in both $SPT^{C133W}$ and Ala-fed cells. The SD of $GP_{ER}$ across all pixels within a single cell was computed for the same cells analyzed in D. **, $p < 0.01$ by Mann-Whitney test.

(F) Cells treated with the CERT inhibitor HPA-12 show increased $GP_{ER}$ (plot on left) and regions of high order tubules (micrographs on right). ****, $p < 0.001$ by Mann-Whitney test.

(G) Membrane fluidity decreases along the secretory pathway in RPE-1, measured by Laurdan GP when segmented with ER (mCherry-Sec61β), Golgi (SiT-mApple), and PM (cell mask deep red) markers.

(H) In $SPT^{C133W}$ cells, the increase in ordering reflected between $GP_{ER}$ and $GP_{Golgi}$ is lost.

(I) Ala-fed cells retain an ER to Golgi GP difference, despite increases in $GP_{ER}$. Points show mean and SEM of individual cell organelle GP; n, $SPT^{WT}$ = 24 (ER), 18 (Golgi), 8 (PM); n, $SPT^{C133W}$ = 20 (ER), 15 (Golgi), 8 (PM); n, RPE-1 = 15 (ER), 12 (Golgi), 4 (PM); n, Ala = 17 (ER), 10 (Golgi), 8 (PM). **, $p < 0.01$; ***, $p < 0.001$; ****, $p < 0.0001$ by two-way ANOVA.

(Figure 4G). $SPT^{C133W}$ cells showed an increase in $GP_{ER}$ but did not show an increase in ordering of Golgi membranes ($GP_{Golgi}$) or the PM ($GP_{PM}$) (Figure 4H). This caused $SPT^{C133W}$ cells to show similar $GP_{ER}$ and $GP_{Golgi}$ values, while the gradient between $GP_{Golgi}$ and $GP_{PM}$ remained unchanged. In contrast, $SPT^{WT}$ cells retained an ordering gradient between ER and Golgi membranes, albeit a reduced one compared to RPE-1 cells. Ala-fed cells maintained a difference between $GP_{ER}$ and $GP_{Golgi}$, despite an increase in the latter (Figure 4I).

Because PennGreen-labeled 1-deoxySLs were enriched at ERES (Figure 2F), we asked if their overproduction in $SPT^{C133W}$ cells alters these structures or their coat proteins. To measure ERES size, we quantified the area occupied by the inner coat protein mCherry-Sec23 in transfected cells. We observed an apparent increase in ERES size in $SPT^{C133W}$ cells compared to both $SPT^{WT}$ and RPE-1 controls (Figure 5A). We did not observe an increase in Ala-fed cells (Figure 5B), suggesting another phenotype that might require high levels of ER-trapped 1-deoxySLs. Immunofluorescence showed patches of the outer coat protein SEC31 in $SPT^{C133W}$ cells that contrasted with discrete and dispersed SEC31 puncta in $SPT^{WT}$ (Figure S5A). Levels of SEC31 across cells were also higher in $SPT^{C133W}$ cells

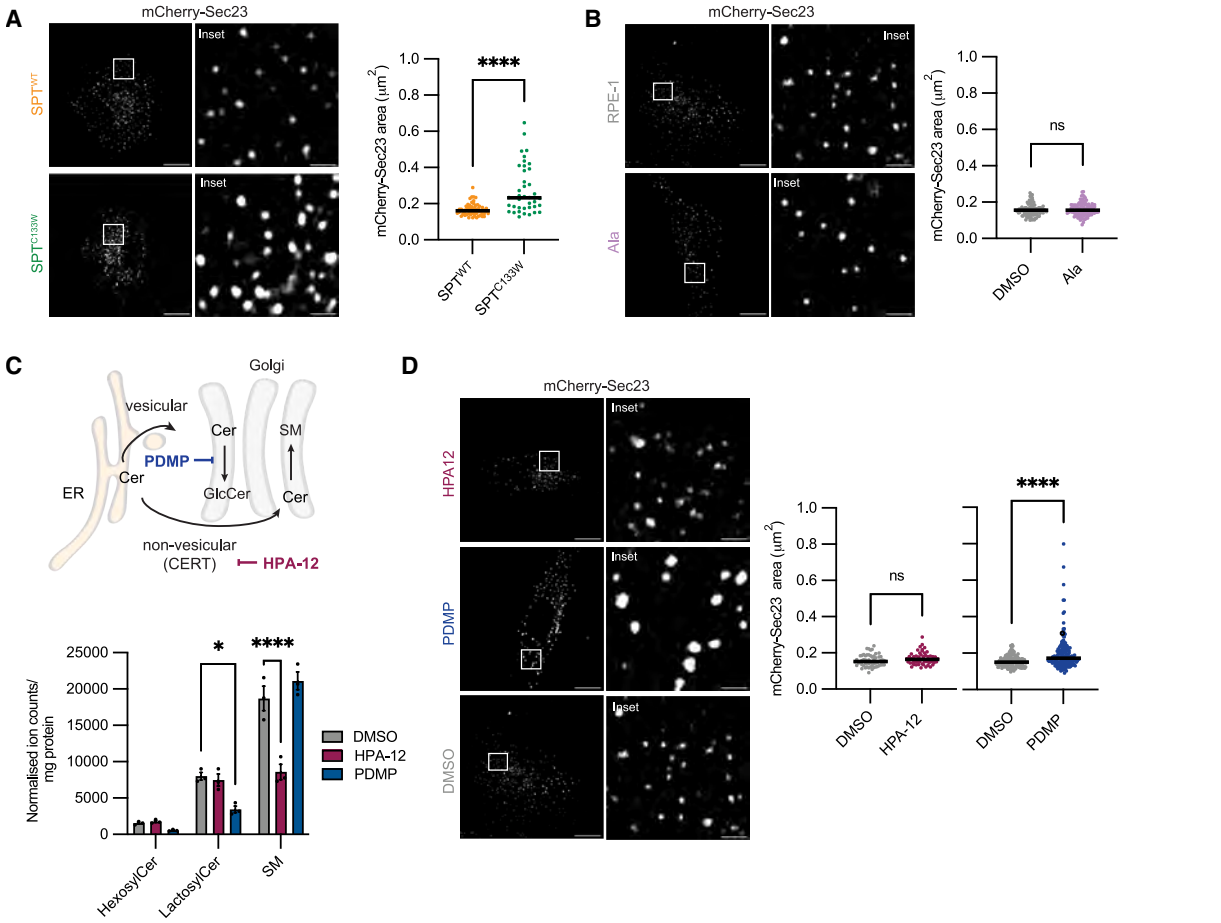


**Figure 5. Alterations to SL metabolism alter ER exit site morphology**

(A) Individual SPT$^{WT}$ and SPT$^{C133W}$ cells transfected with mCherry-Sec23; the latter shows enlarged ERES (0.23 vs. 0.16 μm$^2$) as measured by mCherry-Sec23 area. For the plot on the right, each individual point represents a mCherry-Sec23 puncta; $n$ = 60 sites across 10 cells (SPT$^{WT}$), 40 across 11 cells (SPT$^{C133W}$).

(B) Ala-treated cells show an identical mCherry-Sec23 area (0.15 μm$^2$) as untreated cells (RPE-1, $n$ = 101 across 7 cells; Ala, $n$ = 107 across 12 cells).

(C) The CERT inhibitor HPA-12 inhibits non-vesicular trafficking, leading to a loss of SM. The GCS inhibitor PDMP affects the vesicular trafficking route and leads to a loss of glycosylated SLs.

(D) HPA-12 treatment does not alter ERES size (mean mCherry-Sec23 area of 0.16 μm$^2$ in $n$ = 60 across 15 cells vs. 0.16 μm$^2$ in $n$ = 59 across 15 cells for DMSO-treated control cells), while PDMP does (mean mCherry-Sec23 area of 0.20 μm$^2$ in $n$ = 169 across 20 cells vs. 0.16 μm$^2$ in $n$ = 151 across 16 cells for DMSO-treated control cells). *, $p < 0.05$; ****, $p < 0.001$ by Mann-Whitney test. Scale bars = 11 μm (whole cell) or 1.5 μm (inset).

(Figure S5B), suggesting an additional factor that could affect coat protein localization.

We asked if alterations to ERES structure and/or composition result from the properties of 1-deoxySLs or their failure to traffic out of the ER. In RPE-1, we inhibited both routes for ER trafficking and processing of ceramides: the SM pathway through CERT inhibition (HPA-12), and the vesicular pathway through the inhibition of glucosylceramide synthase (GCS) with PDMP.[55] HPA-12-treated cells showed lower accumulation of SM, while PDMP reduced hexosyl and lactosyl Cers, consistent with the distinct branches of post-ceramide SL metabolism (Figure 5C). Only PDMP treatment caused an apparent enlargement in the mCherry-Sec23 area (Figure 5D), indicating that the GCS pathway in SL metabolism is tied to vesicular trafficking. This observation further supports a model in which defects in the vesicular trafficking of 1-deoxySLs could drive their accumulation in ERES (Figure 2F) and thus affect these structures in cells (Figure 5A).

## 1-deoxysphingolipids cause cargo-specific effects on secretory trafficking

A gradient of membrane ordering has been proposed to function in driving directionality and sorting of secretory cargoes at both the ER and Golgi.[56,57] Recently, it was observed that the reduction of ER membrane fluidity sped up release of cargoes preferring disordered membranes (TNF-α) to the Golgi, while those preferring ordered membrane environments (GPI-anchored proteins) were slowed down.[58] We tested if 1-deoxySLs could act through this mechanism using Retention Using Selective Hooks (RUSH) assay to correlate changes to secretory pathway ordering to cargo trafficking rates[59] (Figure 6A). In these experiments, the addition of biotin to cells causes the dissociation of

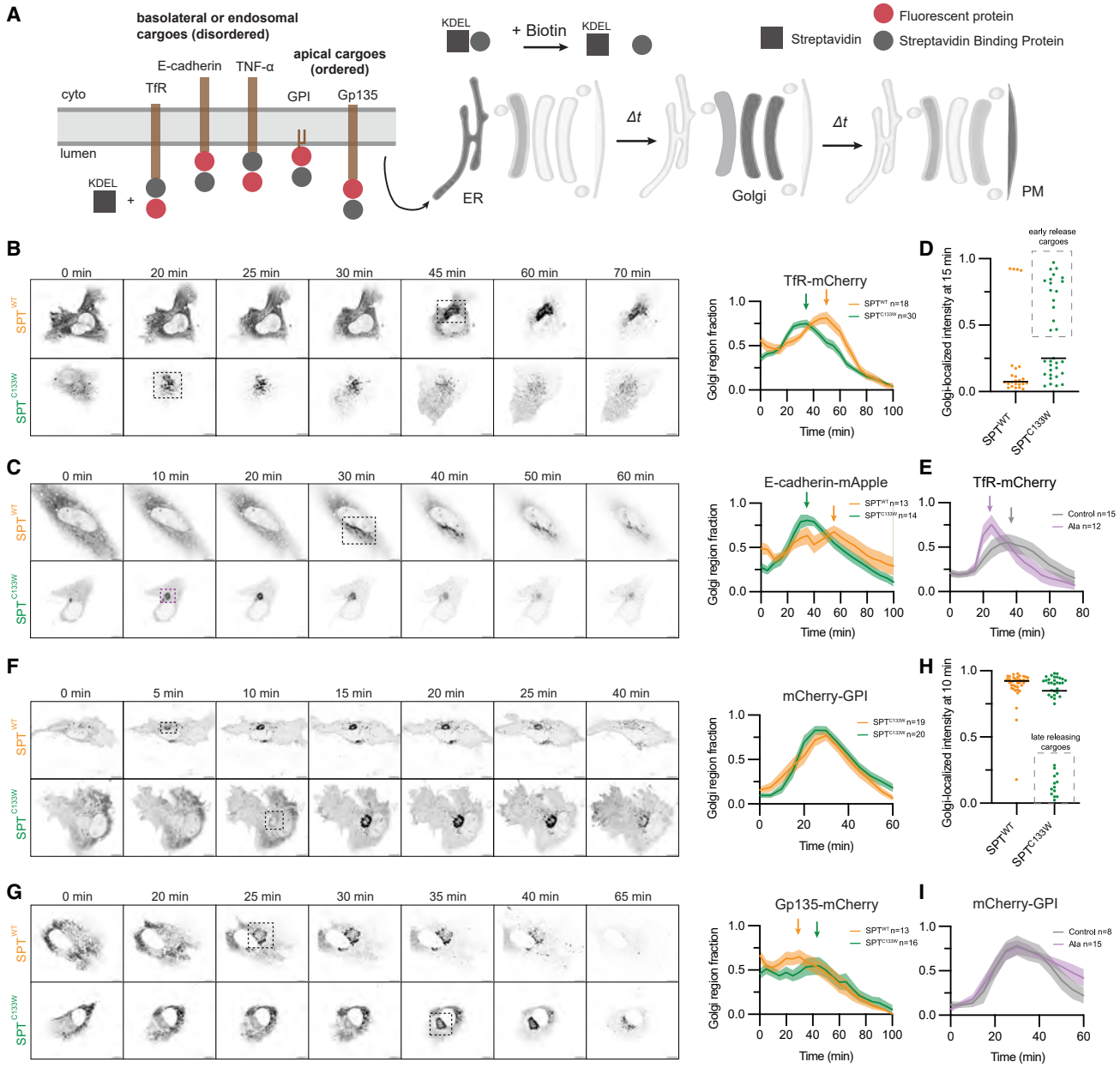


**Figure 6. Accumulation of 1-deoxySLs modulates protein cargo release from the ER**

(A) RUSH experiments for monitoring release of different protein cargoes from the ER through the Golgi.

(B) Representative time course comparing ER release of TfR-mCherry upon biotin addition in $SPT^{WT}$ and $SPT^{C133W}$ cells. Dashed boxes indicate quantified Golgi regions; they are shown at the time point corresponding to the initial Golgi accumulation observed. The plot on the right shows cargo intensity within Golgi regions as a fraction of the whole cell. Arrows indicate times for maximum cargo concentration in the Golgi region. Number of cells (n) for each condition is provided. Scale bars,10 μm.

(C) Similar data for the basolateral membrane protein E-cadherin-mApple.

(D) Fixed cell RUSH experiments with TfR show an early release population co-localizing with the Golgi marker in $SPT^{C133W}$ cells at 15 min. Time course data is shown in Figure S6C, alongside that of another disordered membrane cargo (TNF-α-mCherry).

(E) Ala-supplemented cells also show an early release of TfR-mCherry.

(F) Representative live cell time course for ER release of GPI-anchored mCherry. In this case, maximum Golgi-region intensity occurs at a similar time for both $SPT^{WT}$ and $SPT^{C133W}$ cells, but the former shows increased levels at early time points. Scale bars, 10 μm.

(G) Similar data for the apical transmembrane protein Gp135, which shows slower ER exit kinetics in $SPT^{C133W}$ cells. (H) Fixed cell RUSH data show a population of $SPT^{C133W}$ cells with unreleased mCherry-GPI at 10 min after biotin addition. Time course data are shown in Figure S6D.

(I) Ala-supplemented cells show identical mCherry-GPI ER release kinetics.

the cargoes fused to a streptavidin-binding protein (SBP) from an ER-localized hook containing a streptavidin fused to a KDEL sequence. We focused on anterograde transport from the ER to the Golgi, given that the differences across these compartments showed the largest change from our experimental perturbations.

We first analyzed two single-pass transmembrane proteins: transferrin receptor (TfR-mCherry) and E-cadherin (E-cadherin-mApple) with live cell RUSH assays, in which accumulation to perinuclear-Golgi regions is quantified. TfR is an internalized receptor that cycles between the PM and endosomes, while E-cadherin is a cell-cell adhesion protein that localizes to basolateral membranes in polarized cells; both cargoes associate with liquid-disordered regions of phase-separated giant plasma membrane vesicles (GPMVs), indicating an affinity for disordered membrane environments.[60] For both, we observed moderately more rapid trafficking from the ER to Golgi in $SPT^{C133W}$ compared to $SPT^{WT}$ in live cell experiments (Figures 6B and 6C). We confirmed these results in fixed-cell RUSH experiments with TfR, in which Golgi-localization is assessed through co-localization with GM130 (Figure S6A). Another disordered cargo, TNF-α-mCherry, also showed more rapid ER release in $SPT^{C133W}$ cells in these experiments (Figure S6C). Since fixed cell RUSH experiments allow the analysis of a larger number of cells, they allowed us to identify a fast-release population of $SPT^{C133W}$ cells in which TfR is released within 15 min of biotin addition (Figure 6D). Ala-fed cells also showed more rapid TfR release compared to RPE-1 controls, further supporting a role for 1-deoxySLs in altering ER release kinetics for this cargo (Figure 6E).

We next tested a pair of apical membrane cargoes, a GPI-anchored protein (mCherry-GPI)[61] and the transmembrane protein Gp135.[62] These proteins localize to liquid ordered regions of GPMVs[63] and exit the ER faster than disordered cargoes.[64] In yeast, the sorting of GPI-anchored proteins to COPII vesicles for ER exit depends on sphingolipids,[65,66] though the extent this is true for mammalian cells is debated.[67] For mCherry-GPI, we observed $SPT^{C133W}$ cells did not show the enhanced secretion displayed for disordered cargoes (Figure 6F) and cells showed a late release population absent in $SPT^{WT}$ (Figure 6H). For Gp135, $SPT^{C133W}$ cells showed slowed release kinetics compared to $SPT^{WT}$. Analysis of larger populations of cells at discrete timepoints in fixed cell RUSH experiments also revealed a slowed release of mCherry-GPI in $SPT^{C133W}$ compared to $SPT^{WT}$ and RPE-1 (Figure S6B) and showed that sub-populations of $SPT^{C133W}$ cells retained ER localization after release had been completed in $SPT^{WT}$ cells (Figure 6H). Ala-supplemented cells, which also accumulate 1-deoxySLs, though to a lesser extent than $SPT^{C133W}$-expressing cells, also did not show any changes to mCherry-GPI secretion rates (Figure 6I). In the systems tested, the accumulation of 1-deoxySLs either slows ER exit kinetics of apical membrane cargoes or leaves them unchanged. In contrast, they increased the rate of ER exit for disordered membrane cargoes.

## DISCUSSION

Since their discovery as a disease-associated lipid class, there have been efforts to identify cytotoxic roles for 1-deoxySLs. While such roles are certainly possible, the tissue-specific nature of genetic disorders caused by SPT mutations suggests that more nuanced effects could also be relevant for their pathology. Here, we used a combination of approaches to better understand the role of 1-deoxySLs in an RPE cell line that is a commonly used model for secretory pathway biology. We propose that 1-deoxySLs are largely retained in the ER, where they alter the structure and membrane properties of this organelle, which can affect the function of this organelle in the secretory pathway.

Canonical Cers are transported from the ER to the Golgi via vesicular and non-vesicular trafficking, with the latter mediated by CERT. We initially suspected that CERT-mediated transport of 1-deoxyCer could be impeded, since the START domain of CERT makes direct polar contacts with the C1 hydroxyl of Cer. However, recombinant CERT START domain can transport a model 1-deoxySL *in vitro*, and in fact does so at a higher rate than its corresponding DHCer species. Two additional lines of evidence support that the vesicular trafficking of 1-deoxySL could be impaired. First, 1-deoxySLs accumulate at or near ERES, indicating that they might not be efficiently trafficked through anterograde carriers. Second, overproduction of 1-deoxySLs by $SPT^{C133W}$ cells causes the alteration of ERES structure. We observed similar effects in non-1-deoxySL producing cells whose glucosylceramide synthase is inhibited, reflecting a potential backup of canonical Cer trafficking through ERES to the *cis*-Golgi. Limited vesicular trafficking of 1-deoxySLs could result from effects on anterograde vesicle formation itself or from the inability of SL metabolism to subsequently modify 1-deoxy products.

Even though CERT transports 1-deoxyDHCer *in vitro*, non-vesicular transport of 1-deoxy cargoes might still be limited in cells. We observed that 1-deoxyCer and 1-deoxyDHCers produced in RPE-1 primarily contain VLCFA *N*-acyl chains greater than 20 carbons in length. Enrichment of VLCA chains in 1-deoxy species had been previously reported in RAW macrophages[7] and HCT116 colorectal cancer cells,[31] suggesting that it is a general feature determined by the differing substrate specificities of ceramide synthases (CerS), such as CerS2[68] and CerS5.[69] VLCFA-containing Cers are less efficiently transported by CERT,[70] which could underlie the role of CERT in mediating their transport to the *trans*-Golgi for conversion into short N-acyl chain SM by SMS1. In contrast, it was proposed that VLCFA-containing ceramides are sorted into vesicular carriers for ER export,[71] where they are delivered to the *cis*-Golgi for GCS. Our data suggest that 1-deoxyCer and 1-deoxyDHCer could operate under similar constraints.

The lack of a polar group on the backbone of 1-deoxySLs alters their biophysical properties, namely their hydrophobicity and immiscibility with other lipids. In our experience, both 1-deoxyCers and 1-deoxyDHCers are challenging to even reconstitute into synthetic liposomes using standard protocols. Cell-synthesized 1-deoxySLs are enriched in VLCFA *N*-acyl chains, which would further contribute to these properties. In the context of a highly fluid ER membrane, the accumulation of long-chain saturated or monounsaturated Cer/DHCer species could dramatically alter membrane properties. We observe reduced levels of membrane fluidity in 1-deoxySL producing cells. It is still unclear if this reflects a uniformly more ordered membrane or the formation of localized ordered domains.

Laurdan shows low fluorescence in solid, gel-like domains,[72] which ceramides[73] and their 1-deoxy analogues[8] readily form, so it is possible that our analysis does not fully capture these effects. The increase in ER Laurdan GP (reduced fluidity) caused by 1-deoxySL synthesis can be replicated by the inhibition of canonical Cer trafficking (via CERT inhibition). Although both 1-deoxySLs and Cer accumulate at low abundances in cells (<10 mol % of all lipids), these data suggest that they can still act as potent manipulators of membrane properties. Additional efforts are required to fully elucidate key biophysical functions that our data suggest and the relevant cellular concentrations required to induce them.

In cells that accumulate large amounts of 1-deoxySLs, the ER shows similar membrane ordering as Golgi membranes, which could interfere with long-proposed biophysical gradients across the secretory pathway.[74] A wide range of studies have shown that membrane domains or anchors of secreted proteins could be matched to their host lipid bilayer to maintain proper sorting during secretion.[64,75–77] In polarized cells, PM proteins are thought to segregate by a similar mechanism, potentially at endosomes,[78] with basolateral proteins matching with more disordered membranes and apical proteins with more ordered, raft-like membranes.[79,80] The latter are enriched in SLs and cholesterol.[81] While comparative studies on different membrane proteins have shed light on their secretory trafficking, how lipid perturbations affect this process is less explored. An exception is the post-Golgi sorting of apical and basolateral membrane proteins.[82,83] More recently, the disruption of the ER to *trans*-Golgi cholesterol transport carried out by oxysterol binding protein (OSBP) has been shown to alter apical vs. basolateral cargo secretion.[84] Much like SLs, cholesterol forms an increasing gradient along the secretory pathway, despite its synthesis in the ER due to highly active export pathways.[85]

Cargo export from the ER itself could also be dependent on changes in secretory pathway membrane ordering, as suggested by reported effects on reduced SL synthesis inhibition upon myriocin treatment[58] or knockdown of ether lipid synthesis.[86] One model for these effects is that cargo sorting into the ERES itself is dependent on its bilayer mismatch with the rest of the ER matrix. Apical cargoes, such as GPI-anchored proteins, rapidly sort into ERES, potentially due to their lipid microenvironment that better reflects the plasma membrane. It has recently been shown that the sorting of such cargoes into ERES is slowed when ER membrane ordering is increased.[58] Through this mechanism, an increase in ER membrane ordering caused by failure of 1-deoxySLs to exit the ER could reduce cargoes' affinity for ERES foci, leading to higher diffusion through the ER network. In contrast, cargoes tailored for thinner and more disordered membranes may not match with more ordered ER membranes caused by 1-deoxySLs, accelerating their sorting toward ERES. Such a model depends on the existence of multiple classes of exit carriers for different types of cargoes, which has long been hypothesized.[87,88] In some cells, ERES are interconnected with the *cis*-Golgi, suggesting that they might approximate the more ordered state of that compartment.[45] An outstanding question is if 1-deoxySL themselves are also quickly transported through exit sites – and then presumably trafficked back to the ER through retrograde trafficking – or inhibit carrier release and thus accumulate there.

Given their substantial effects on the packing of lipid membranes and their disparate membrane concentrations, we propose that the dysregulation of SL homeostasis could be especially relevant for the processing of proteins through the secretory pathway. The pathophysiology of SL-related diseases, including those that affect degradation,[89] and trafficking,[90] remains mysterious. In the case of diseases that are thought to be driven by increased 1-deoxy bases, effects on the trafficking of specific membrane protein cargoes could be relevant for understanding their cellular targets. For MacTel, sorting of proteins is required to support the polarized proteome of RPE that support photoreceptors. In HSAN1, axonal neuropathy is accompanied by the loss of myelin, a structure enriched in secreted SLs and membrane proteins with affinities for ordered membrane.[91] The retention of 1-deoxySL products within early secretory compartments could disrupt both these processes and contribute to cell type-specific pathologies that depend on the trafficking of individual membrane proteins synthesized in the ER. Similar dynamics could be relevant for other diseases related to the SL metabolism and transport.

### Limitations of this study

While 1-deoxySL metabolites are observed to accumulate at the ER, the molecular composition and absolute abundance of this ER pool is not detailed. Doing so requires advancements in 1-deoxySL analysis and further subcellular fractionation. The exact effects of 1-deoxySLs on membrane properties in the ER or in model systems are also not yet resolved. Observed effects of 1-deoxySL overproduction on ERES could result from changes to their morphology, recruitment of coat proteins, or alterations to their release; delineating these roles requires further ultrastructural analysis. While effects on the secretion of apical and basolateral membrane proteins are observed, it has not yet been demonstrated that 1-deoxySLs can alter the display of relevant surface receptors in polarized epithelium.

## RESOURCE AVAILABILITY

### Lead contact

Further information and requests for resources and reagents should be directed to and will be fulfilled by the lead contact, Itay Budin (ibudin@ucsd.edu).

### Materials availability

Cell lines, plasmids, and reagents are freely available upon request from the lead contact with a materials transfer agreement as long as stocks remain available.

### Data and code availability

- All data reported in this article will be shared by the lead contact upon request.
- Python scripts for Laurdan GP analysis from microscopy data are archived at Zenodo (https://doi.org/10.5281/zenodo.17874908).
- Any additional information required to reanalyze the data reported in this article is available from the lead contact upon request.

## ACKNOWLEDGMENTS

Dorota Skowronska-Krawczyk, Chris Obara, Aubrey Weigel, Ivan Castello-Serrano, and David Kovács provided helpful discussions. Kailash Venkatraman and Elida Kocharian provided experimental support. Dorota

Skowronska-Krawczyk and Jennifer Lipincott-Schwartz provided reagents. Funding was provided by the National Institutes of Health (R35-GM142960 to I.B., R01-CA234245 to C.M.M., R35-GM141939 to N.K.D., R35-GM133565 to S.N., T32-GM139795 to O.S., T32-GM146648 to A.W.), the National Science Foundation (MCB-2047391 to S.N.), HHMI (Freeman Hrabowski Scholar Program to S.N.), and MCIN/AEI/10.13039/501100011033 and ERDF A way of making Europe (RYC2020-030065-I to R.J.B.).

## AUTHOR CONTRIBUTIONS

Y-T.T., C.M.M., and I.B. conceived the project. Y-T.T., N-F.L., O.S., A. L., K.S-K., and G.H.M carried out experiments. R.V. analyzed data. A.W., O.S., and R.J.B. synthesized reagents. N.K.D., L.K., S.N., C.M.M., and I.B. supervised the project and acquired funding. Y-T.T., N-F.L., O.S., A.L., K.S-K., R.J.B., and I.B. wrote the article. All authors revised the article.

## DECLARATION OF INTERESTS

The authors declare no competing interests.

## STAR★METHODS

Detailed methods are provided in the online version of this paper and include the following:

- KEY RESOURCES TABLE
- EXPERIMENTAL MODEL AND STUDY PARTICIPANT DETAILS
- METHOD DETAILS
  - Synthesis of new compounds
  - Cell line generation and analysis
  - Imaging
  - Biochemistry
  - Lipid mass spectrometry
- QUANTIFICATION AND STATISTICAL ANALYSIS

## SUPPLEMENTAL INFORMATION

Supplemental information can be found online at https://doi.org/10.1016/j.chembiol.2025.12.006.

Received: May 13, 2025
Revised: November 24, 2025
Accepted: December 10, 2025
Published: January 15, 2026

## REFERENCES

1. Wang, Y., Niu, Y., Zhang, Z., Gable, K., Gupta, S.D., Somashekarappa, N., Han, G., Zhao, H., Myasnikov, A.G., and Kalathur, R.C. (2021). Structural insights into the regulation of human serine palmitoyltransferase complexes. Nat. Struct. Mol. Biol. *28*, 240–248.
2. Yamaji, T., and Hanada, K. (2015). Sphingolipid metabolism and interorganellar transport: localization of sphingolipid enzymes and lipid transfer proteins. Traffic *16*, 101–122.
3. Monasterio, B.G., Jiménez-Rojo, N., García-Arribas, A.B., Riezman, H., Goñi, F.M., and Alonso, A. (2022). Plasma membrane effects of sphingolipid-synthesis inhibition by myriocin in CHO cells: a biophysical and lipidomic study. Sci. Rep. *12*, 955.
4. Steiner, R., Saied, E.M., Othman, A., Arenz, C., Maccarone, A.T., Poad, B.L.J., Blanksby, S.J., von Eckardstein, A., and Hornemann, T. (2016). Elucidating the chemical structure of native 1-deoxysphingosine. J. Lipid Res. *57*, 1194–1203.
5. Alecu, I., Othman, A., Penno, A., Saied, E.M., Arenz, C., von Eckardstein, A., and Hornemann, T. (2017). Cytotoxic 1-deoxysphingolipids are metabolized by a cytochrome P450-dependent pathway. J. Lipid Res. *58*, 60–71.
6. Lone, M.A., Santos, T., Alecu, I., Silva, L.C., and Hornemann, T. (2019). 1-Deoxysphingolipids. Biochim. Biophys. Acta. Mol. Cell Biol. Lipids *1864*, 512–521.
7. Jiménez-Rojo, N., Sot, J., Busto, J.V., Shaw, W.A., Duan, J., Merrill, A.H., Jr., Alonso, A., and Goñi, F.M. (2014). Biophysical properties of novel 1-deoxy-(dihydro)ceramides occurring in mammalian cells. Biophys. J. *107*, 2850–2859.
8. González-Ramírez, E.J., García-Arribas, A.B., Artetxe, I., Shaw, W.A., Goñi, F.M., Alonso, A., and Jiménez-Rojo, N. (2024). (1-Deoxy)ceramides in bilayers containing sphingomyelin and cholesterol. Colloids Surf. B Biointerfaces *243*, 114155.
9. Cuadros, R., Montejo de Garcini, E., Wandosell, F., Faircloth, G., Fernández-Sousa, J.M., and Avila, J. (2000). The marine compound spisulosine, an inhibitor of cell proliferation, promotes the disassembly of actin stress fibers. Cancer Lett. *152*, 23–29.
10. Marasas, W.F. (2001). Discovery and occurrence of the fumonisins: a historical perspective. Environ. Health Perspect. *109*, 239–243.
11. Zitomer, N.C., Mitchell, T., Voss, K.A., Bondy, G.S., Pruett, S.T., Garnier-Amblard, E.C., Liebeskind, L.S., Park, H., Wang, E., Sullards, M.C., et al. (2009). Ceramide Synthase Inhibition by Fumonisin B1 Causes Accumulation of 1-Deoxysphinganine: A Novel Category of Bioactive 1-Deoxysphingoid Bases And 1-Deoxydihydroceramides Biosynthesized by Mammalian Cell Lines and Animals. J. Biol. Chem. *284*, 4786–4795.
12. Othman, A., Saely, C.H., Muendlein, A., Vonbank, A., Drexel, H., von Eckardstein, A., and Hornemann, T. (2015). Plasma 1-deoxysphingolipids are predictive biomarkers for type 2 diabetes mellitus. BMJ Open Diabetes Res. Care *3*, e000073.
13. Dohrn, M.F., Othman, A., Hirshman, S.K., Bode, H., Alecu, I., Fähndrich, E., Karges, W., Weis, J., Schulz, J.B., Hornemann, T., and Claeys, K.G. (2015). Elevation of plasma 1-deoxy-sphingolipids in type 2 diabetes mellitus: a susceptibility to neuropathy? Eur. J. Neurol. *22*, 806–814.e55.
14. Penno, A., Reilly, M.M., Houlden, H., Laurá, M., Rentsch, K., Niederkofler, V., Stoeckli, E.T., Nicholson, G., Eichler, F., Brown, R.H., et al. (2010). Hereditary Sensory Neuropathy Type 1 Is Caused by the Accumulation of Two Neurotoxic Sphingolipids. J. Biol. Chem. *285*, 11178–11187.
15. Bode, H., Bourquin, F., Suriyanarayanan, S., Wei, Y., Alecu, I., Othman, A., Von Eckardstein, A., and Hornemann, T. (2016). HSAN1 mutations in serine palmitoyltransferase reveal a close structure-function-phenotype relationship. Hum. Mol. Genet. *25*, 853–865.
16. McCampbell, A., Truong, D., Broom, D.C., Allchorne, A., Gable, K., Cutler, R.G., Mattson, M.P., Woolf, C.J., Frosch, M.P., Harmon, J.M., et al. (2005). Mutant SPTLC1 dominantly inhibits serine palmitoyltransferase activity *in vivo* and confers an age-dependent neuropathy. Hum. Mol. Genet. *14*, 3507–3521.
17. Eichler, F.S., Hornemann, T., McCampbell, A., Kuljis, D., Penno, A., Vardeh, D., Tamrazian, E., Garofalo, K., Lee, H.-J., Kini, L., et al. (2009). Overexpression of the wild-type SPT1 subunit lowers desoxysphingolipid levels and rescues the phenotype of HSAN1. J. Neurosci. *29*, 14646–14651.
18. Gantner, M.L., Eade, K., Wallace, M., Handzlik, M.K., Fallon, R., Trombley, J., Bonelli, R., Giles, S., Harkins-Perry, S., Heeren, T.F.C., et al. (2019). Serine and Lipid Metabolism in Macular Disease and Peripheral Neuropathy. N. Engl. J. Med. *381*, 1422–1433.
19. Scerri, T.S., Quaglieri, A., Cai, C., Zernant, J., Matsunami, N., Baird, L., Scheppke, L., Bonelli, R., Yannuzzi, L.A., Friedlander, M., et al. (2017). Genome-wide analyses identify common variants associated with macular telangiectasia type 2. Nat. Genet. *49*, 559–567.
20. Cherepanoff, S., Killingsworth, M.C., Zhu, M., Nolan, T., Hunyor, A.P., Young, S.H., Hageman, G.S., and Gillies, M.C. (2012). Ultrastructural and clinical evidence of subretinal debris accumulation in type 2 macular telangiectasia. Br. J. Ophthalmol. *96*, 1404–1409.
21. Chen, L., Messinger, J.D., Zhang, Y., Spaide, R.F., Freund, K.B., and Curcio, C.A. (2020). Subretinal Drusenoid Deposit in Age-Related Macular Degeneration: Histologic Insights Into Initiation, Progression to Atrophy, and Imaging. Retina *40*, 618–631.

22. Powner, M.B., Woods, S.M., Zhu, M., Gillies, M.C., Bernstein, P.S., Hageman, G.S., Comer, G.M., Egan, C., and Fruttiger, M. (2018). Fundus-Wide Subretinal and Pigment Epithelial Abnormalities in Macular Telangiectasia Type 2. Retina *38*, S105–S113.

23. Feng, W., Yasumura, D., Matthes, M.T., LaVail, M.M., and Vollrath, D. (2002). Mertk triggers uptake of photoreceptor outer segments during phagocytosis by cultured retinal pigment epithelial cells. J. Biol. Chem. *277*, 17016–17022.

24. Alecu, I., Tedeschi, A., Behler, N., Wunderling, K., Lamberz, C., Lauterbach, M.A.R., Gaebler, A., Ernst, D., Van Veldhoven, P.P., Al-Amoudi, A., et al. (2017). Localization of 1-deoxysphingolipids to mitochondria induces mitochondrial dysfunction. J. Lipid Res. *58*, 42–59.

25. Sánchez, A.M., Malagarie-Cazenave, S., Olea, N., Vara, D., Cuevas, C., and Díaz-Laviada, I. (2008). Spisulosine (ES-285) induces prostate tumor PC-3 and LNCaP cell death by *de novo* synthesis of ceramide and PKCzeta activation. Eur. J. Pharmacol. *584*, 237–245.

26. Güntert, T., Hänggi, P., Othman, A., Suriyanarayanan, S., Sonda, S., Zuellig, R.A., Hornemann, T., and Ogunshola, O.O. (2016). 1-Deoxysphingolipid-induced neurotoxicity involves N-methyl-d-aspartate receptor signaling. Neuropharmacology *110*, 211–222.

27. Rosarda, J.D., Giles, S., Harkins-Perry, S., Mills, E.A., Friedlander, M., Wiseman, R.L., and Eade, K.T. (2023). Imbalanced unfolded protein response signaling contributes to 1-deoxysphingolipid retinal toxicity. Nat. Commun. *14*, 4119.

28. Salcedo, M., Cuevas, C., Alonso, J.L., Otero, G., Faircloth, G., Fernandez-Sousa, J.M., Avila, J., and Wandosell, F. (2007). The marine sphingolipid-derived compound ES 285 triggers an atypical cell death pathway. Apoptosis *12*, 395–409.

29. Lauterbach, M.A., Saavedra, V., Mangan, M.S.J., Penno, A., Thiele, C., Latz, E., and Kuerschner, L. (2021). 1-Deoxysphingolipids cause autophagosome and lysosome accumulation and trigger NLRP3 inflammasome activation. Autophagy *17*, 1947–1961.

30. Kamp, F., and Hamilton, J.A. (2006). How fatty acids of different chain length enter and leave cells by free diffusion. Prostaglandins Leukot. Essent. Fatty Acids *75*, 149–159.

31. Cordes, T., Kuna, R.S., McGregor, G.H., Khare, S.V., Gengatharan, J., Muthusamy, T., and Metallo, C.M. (2022). 1-Deoxysphingolipid synthesis compromises anchorage-independent growth and plasma membrane endocytosis in cancer cells. J. Lipid Res. *63*, 100281.

32. Myers, S.J., Malladi, C.S., Hyland, R.A., Bautista, T., Boadle, R., Robinson, P.J., and Nicholson, G.A. (2014). Mutations in the SPTLC1 protein cause mitochondrial structural abnormalities and endoplasmic reticulum stress in lymphoblasts. DNA Cell Biol. *33*, 399–407.

33. Jao, C.Y., Roth, M., Welti, R., and Salic, A. (2009). Metabolic labeling and direct imaging of choline phospholipids *in vivo*. Proc. Natl. Acad. Sci. USA *106*, 15332–15337.

34. Meinig, J.M., Fu, L., and Peterson, B.R. (2015). Synthesis of fluorophores that target small molecules to the endoplasmic reticulum of living mammalian cells. Angew. Chem. Int. Ed. Engl. *54*, 9696–9699.

35. Tamura, T., Fujisawa, A., Tsuchiya, M., Shen, Y., Nagao, K., Kawano, S., Tamura, Y., Endo, T., Umeda, M., and Hamachi, I. (2020). Organelle membrane-specific chemical labeling and dynamic imaging in living cells. Nat. Chem. Biol. *16*, 1361–1367.

36. Fujisawa, A., Tamura, T., Yasueda, Y., Kuwata, K., and Hamachi, I. (2018). Chemical profiling of the endoplasmic reticulum proteome using designer labeling reagents. J. Am. Chem. Soc. *140*, 17060–17070.

37. Gaebler, A., Penno, A., Kuerschner, L., and Thiele, C. (2016). A highly sensitive protocol for microscopy of alkyne lipids and fluorescently tagged or immunostained proteins. J. Lipid Res. *57*, 1934–1947.

38. Kok, J.W., Nikolova-Karakashian, M., Klappe, K., Alexander, C., and Merrill, A.H. (1997). Dihydroceramide Biology: STRUCTURE-SPECIFIC METABOLISM AND INTRACELLULAR LOCALIZATION. J. Biol. Chem. *272*, 21128–21136.

39. Hanada, K., Kumagai, K., Yasuda, S., Miura, Y., Kawano, M., Fukasawa, M., and Nishijima, M. (2003). Molecular machinery for non-vesicular trafficking of ceramide. Nature *426*, 803–809.

40. Kumagai, K., and Hanada, K. (2019). Structure, functions and regulation of CERT, a lipid-transfer protein for the delivery of ceramide at the ER-Golgi membrane contact sites. FEBS Lett. *593*, 2366–2377.

41. Funakoshi, T., Yasuda, S., Fukasawa, M., Nishijima, M., and Hanada, K. (2000). Reconstitution of ATP- and cytosol-dependent transport of *de novo* synthesized ceramide to the site of sphingomyelin synthesis in semi-intact cells. J. Biol. Chem. *275*, 29938–29945.

42. Ikhlef, S., Lipp, N.-F., Delfosse, V., Fuggetta, N., Bourguet, W., Magdeleine, M., and Drin, G. (2021). Functional analyses of phosphatidylserine/PI(4)P exchangers with diverse lipid species and membrane contexts reveal unanticipated rules on lipid transfer. BMC Biol. *19*, 248.

43. Giussani, P., Colleoni, T., Brioschi, L., Bassi, R., Hanada, K., Tettamanti, G., Riboni, L., and Viani, P. (2008). Ceramide traffic in C6 glioma cells: evidence for CERT-dependent and independent transport from ER to the Golgi apparatus. Biochim. Biophys. Acta *1781*, 40–51.

44. Funato, K., and Riezman, H. (2001). Vesicular and nonvesicular transport of ceramide from ER to the Golgi apparatus in yeast. J. Cell Biol. *155*, 949–959.

45. Weigel, A.V., Chang, C.-L., Shtengel, G., Xu, C.S., Hoffman, D.P., Freeman, M., Iyer, N., Aaron, J., Khuon, S., Bogovic, J., et al. (2021). ER-to-Golgi protein delivery through an interwoven, tubular network extending from ER. Cell *184*, 2412–2429.e16.

46. Sim, W.-C., Han, I., Lee, W., Choi, Y.-J., Lee, K.-Y., Kim, D.G., Jung, S.-H., Oh, S.-H., and Lee, B.-H. (2016). Inhibition of homocysteine-induced endoplasmic reticulum stress and endothelial cell damage by l-serine and glycine. Toxicol. Vitro *34*, 138–145.

47. Maddocks, O.D.K., Berkers, C.R., Mason, S.M., Zheng, L., Blyth, K., Gottlieb, E., and Vousden, K.H. (2013). Serine starvation induces stress and p53-dependent metabolic remodelling in cancer cells. Nature *493*, 542–546.

48. Dawkins, J.L., Hulme, D.J., Brahmbhatt, S.B., Auer-Grumbach, M., and Nicholson, G.A. (2001). Mutations in SPTLC1, encoding serine palmitoyltransferase, long chain base subunit-1, cause hereditary sensory neuropathy type I. Nat. Genet. *27*, 309–312.

49. Othman, A., Bianchi, R., Alecu, I., Wei, Y., Porretta-Serapiglia, C., Lombardi, R., Chiorazzi, A., Meregalli, C., Oggioni, N., Cavaletti, G., et al. (2015). Lowering plasma 1-deoxysphingolipids improves neuropathy in diabetic rats. Diabetes *64*, 1035–1045.

50. Andreyev, A.Y., Fahy, E., Guan, Z., Kelly, S., Li, X., McDonald, J.G., Milne, S., Myers, D., Park, H., Ryan, A., et al. (2010). Subcellular organelle lipidomics in TLR-4-activated macrophages. J. Lipid Res. *51*, 2785–2797.

51. Tuller, G., Nemec, T., Hrastnik, C., and Daum, G. (1999). Lipid composition of subcellular membranes of an FY1679-derived haploid yeast wild-type strain grown on different carbon sources. Yeast *15*, 1555–1564.

52. Owen, D.M., Rentero, C., Magenau, A., Abu-Siniyeh, A., and Gaus, K. (2011). Quantitative imaging of membrane lipid order in cells and organisms. Nat. Protoc. *7*, 24–35.

53. Yasuda, S., Kitagawa, H., Ueno, M., Ishitani, H., Fukasawa, M., Nishijima, M., Kobayashi, S., and Hanada, K. (2001). A novel inhibitor of ceramide trafficking from the endoplasmic reticulum to the site of sphingomyelin synthesis. J. Biol. Chem. *276*, 43994–44002.

54. Antonny, B., Vanni, S., Shindou, H., and Ferreira, T. (2015). From zero to six double bonds: phospholipid unsaturation and organelle function. Trends Cell Biol. *25*, 427–436.

55. Inokuchi, J., and Radin, N.S. (1987). Preparation of the active isomer of 1-phenyl-2-decanoylamino-3-morpholino-1-propanol, inhibitor of murine glucocerebroside synthetase. J. Lipid Res. *28*, 565–571.

56. Patterson, G.H., Hirschberg, K., Polishchuk, R.S., Gerlich, D., Phair, R.D., and Lippincott-Schwartz, J. (2008). Transport through the Golgi apparatus by rapid partitioning within a two-phase membrane system. Cell *133*, 1055–1067.

57. Klemm, R.W., Ejsing, C.S., Surma, M.A., Kaiser, H.-J., Gerl, M.J., Sampaio, J.L., de Robillard, Q., Ferguson, C., Proszynski, T.J., Shevchenko, A., and Simons, K. (2009). Segregation of sphingolipids and sterols during formation of secretory vesicles at the trans-Golgi network. J. Cell Biol. *185*, 601–612.

58. Jiménez-Rojo, N., Feng, S., Morstein, J., Pritzl, S.D., Asaro, A., López, S., Xu, Y., Harayama, T., Vepřek, N.A., Arp, C.J., et al. (2025). Optical control of membrane viscosity modulates ER-to-Golgi trafficking. ACS Cent. Sci. *11*, 1736–1752.

59. Boncompain, G., Divoux, S., Gareil, N., de Forges, H., Lescure, A., Latreche, L., Mercanti, V., Jollivet, F., Raposo, G., and Perez, F. (2012). Synchronization of secretory protein traffic in populations of cells. Nat. Methods *9*, 493–498.

60. Levental, K.R., and Levental, I. (2015). Isolation of Giant Plasma Membrane Vesicles for Evaluation of Plasma Membrane Structure and Protein Partitioning. In Methods in Membrane Lipids, D.M. Owen, ed. (Springer), pp. 65–77.

61. Lisanti, M.P., Caras, I.W., Davitz, M.A., and Rodriguez-Boulan, E. (1989). A glycophospholipid membrane anchor acts as an apical targeting signal in polarized epithelial cells. J. Cell Biol. *109*, 2145–2156.

62. Meder, D., Shevchenko, A., Simons, K., and Füllekrug, J. (2005). Gp135/podocalyxin and NHERF-2 participate in the formation of a preapical domain during polarization of MDCK cells. J. Cell Biol. *168*, 303–313.

63. Coskun, U., and Simons, K. (2010). Membrane rafting: from apical sorting to phase segregation. FEBS Lett. *584*, 1685–1693.

64. Castello-Serrano, I., Heberle, F.A., Diaz-Rohrer, B., Ippolito, R., Shurer, C.R., Lujan, P., Campelo, F., Levental, K.R., and Levental, I. (2024). Partitioning to ordered membrane domains regulates the kinetics of secretory traffic. eLife *12*, RP89306.

65. Horvath, A., Sütterlin, C., Manning-Krieg, U., Movva, N.R., and Riezman, H. (1994). Ceramide synthesis enhances transport of GPI-anchored proteins to the Golgi apparatus in yeast. EMBO J. *13*, 3687–3695.

66. Watanabe, R., Funato, K., Venkataraman, K., Futerman, A.H., and Riezman, H. (2002). Sphingolipids are required for the stable membrane association of glycosylphosphatidylinositol-anchored proteins in yeast. J. Biol. Chem. *277*, 49538–49544.

67. Rivier, A.-S., Castillon, G.A., Michon, L., Fukasawa, M., Romanova-Michaelides, M., Jaensch, N., Hanada, K., and Watanabe, R. (2010). Exit of GPI-anchored proteins from the ER differs in yeast and mammalian cells. Traffic *11*, 1017–1033.

68. Laviad, E.L., Albee, L., Pankova-Kholmyansky, I., Epstein, S., Park, H., Merrill, A.H., Jr., and Futerman, A.H. (2008). Characterization of ceramide synthase 2: tissue distribution, substrate specificity, and inhibition by sphingosine 1-phosphate. J. Biol. Chem. *283*, 5677–5684.

69. Lahiri, S., and Futerman, A.H. (2005). LASS5 is a bona fide dihydroceramide synthase that selectively utilizes palmitoyl-CoA as acyl donor. J. Biol. Chem. *280*, 33735–33738.

70. Kumagai, K., Yasuda, S., Okemoto, K., Nishijima, M., Kobayashi, S., and Hanada, K. (2005). CERT mediates intermembrane transfer of various molecular species of ceramides. J. Biol. Chem. *280*, 6488–6495.

71. Clausmeyer, L., and Fröhlich, F. (2023). Mechanisms of Nonvesicular Ceramide Transport*6* (Thousand Oaks), pp. 25152564231208250.

72. Celli, A., and Gratton, E. (2010). Dynamics of lipid domain formation: fluctuation analysis. Biochim. Biophys. Acta *1798*, 1368–1376.

73. Goñi, F.M., and Alonso, A. (2009). Effects of ceramide and other simple sphingolipids on membrane lateral structure. Biochim. Biophys. Acta *1788*, 169–177.

74. Bretscher, M.S., and Munro, S. (1993). Cholesterol and the Golgi apparatus. Science *261*, 1280–1281.

75. Sharpe, H.J., Stevens, T.J., and Munro, S. (2010). A comprehensive comparison of transmembrane domains reveals organelle-specific properties. Cell *142*, 158–169.

76. Lorent, J.H., Diaz-Rohrer, B., Lin, X., Spring, K., Gorfe, A.A., Levental, K.R., and Levental, I. (2017). Structural determinants and functional consequences of protein affinity for membrane rafts. Nat. Commun. *8*, 1219. https://doi.org/10.1038/s41467-017-01328-3.

77. Lorent, J.H., Levental, K.R., Ganesan, L., Rivera-Longsworth, G., Sezgin, E., Doktorova, M., Lyman, E., and Levental, I. (2020). Plasma membranes are asymmetric in lipid unsaturation, packing and protein shape. Nat. Chem. Biol. *16*, 644–652.

78. Cresawn, K.O., Potter, B.A., Oztan, A., Guerriero, C.J., Ihrke, G., Goldenring, J.R., Apodaca, G., and Weisz, O.A. (2007). Differential involvement of endocytic compartments in the biosynthetic traffic of apical proteins. EMBO J. *26*, 3737–3748.

79. Stoops, E.H., and Caplan, M.J. (2014). Trafficking to the apical and basolateral membranes in polarized epithelial cells. J. Am. Soc. Nephrol. *25*, 1375–1386.

80. Schuck, S., and Simons, K. (2004). Polarized sorting in epithelial cells: raft clustering and the biogenesis of the apical membrane. J. Cell Sci. *117*, 5955–5964.

81. Simons, K., and van Meer, G. (1988). Lipid sorting in epithelial cells. Biochemistry *27*, 6197–6202.

82. Keller, P., and Simons, K. (1997). Post-Golgi biosynthetic trafficking. J. Cell Sci. *110*, 3001–3009.

83. Paladino, S., Sarnataro, D., Pillich, R., Tivodar, S., Nitsch, L., and Zurzolo, C. (2004). Protein oligomerization modulates raft partitioning and apical sorting of GPI-anchored proteins. J. Cell Biol. *167*, 699–709.

84. Kovács, D., Gay, A.-S., Debayle, D., Abélanet, S., Patel, A., Mesmin, B., Luton, F., and Antonny, B. (2024). Lipid exchange at ER-trans-Golgi contact sites governs polarized cargo sorting. J. Cell Biol. *223*, e202307051. https://doi.org/10.1083/jcb.202307051.

85. Antonny, B., Bigay, J., and Mesmin, B. (2018). The oxysterol-binding protein cycle: Burning off PI(4)P to transport cholesterol. Annu. Rev. Biochem. *87*, 809–837.

86. Jiménez-Rojo, N., Leonetti, M.D., Zoni, V., Colom, A., Feng, S., Iyengar, N.R., Matile, S., Roux, A., Vanni, S., Weissman, J.S., and Riezman, H. (2020). Conserved functions of ether lipids and sphingolipids in the early secretory pathway. Curr. Biol. *30*, 3775–3787.e7.

87. Peng, R., De Antoni, A., and Gallwitz, D. (2000). Evidence for overlapping and distinct functions in protein transport of coat protein Sec24p family members. J. Biol. Chem. *275*, 11521–11528.

88. Wendeler, M.W., Paccaud, J.-P., and Hauri, H.-P. (2007). Role of Sec24 isoforms in selective export of membrane proteins from the endoplasmic reticulum. EMBO Rep. *8*, 258–264.

89. Kolter, T., and Sandhoff, K. (2006). Sphingolipid metabolism diseases. Biochim. Biophys. Acta *1758*, 2057–2079.

90. Gehin, C., Lone, M.A., Lee, W., Capolupo, L., Ho, S., Adeyemi, A.M., Gerkes, E.H., Stegmann, A.P., López-Martín, E., Bermejo-Sánchez, E., et al. (2023). CERT1 mutations perturb human development by disrupting sphingolipid homeostasis. J. Clin. Investig. *133*, e165019. https://doi.org/10.1172/JCI165019.

91. Marinko, J.T., Kenworthy, A.K., and Sanders, C.R. (2020). Peripheral myelin protein 22 preferentially partitions into ordered phase membrane domains. Proc. Natl. Acad. Sci. USA *117*, 14168–14177.

92. Ikhlef, S., Lipp, N.-F., Magdeleine, M., and Drin, G. (2021). Fluorescence-based measurements of phosphatidylserine/phosphatidylinositol 4-phosphate exchange between membranes. J. Vis. Exp. *169*, e62177. https://doi.org/10.3791/62177-v.

93. Bielawski, J., Pierce, J.S., Snider, J., Rembiesa, B., Szulc, Z.M., and Bielawska, A. (2009). Comprehensive quantitative analysis of bioactive sphingolipids by high-performance liquid chromatography-tandem mass spectrometry. Methods Mol. Biol. *579*, 443–467.

## STAR★METHODS

### KEY RESOURCES TABLE

| REAGENT or RESOURCE | SOURCE | IDENTIFIER |
|---|---|---|
| **Antibodies** | | |
| Rabbit anti-SPTLC1 | Proteintech | Cat# 15376-1-AP; RRID: AB_2286678 |
| Mouse anti-β-actin | Cell Signaling Technologies | Cat# 8H10D10; RRID: AB_3212153 |
| rabbit anti-IRE1-phosphorylated | Invitrogen | Cat# PA1-16927; RRID: AB_2262241 |
| rabbit anti-AKT-phosphorylated | Invitrogen | Cat# 44-621G; RRID: AB_2533699 |
| mouse anti-Derlin-1 | Sigma-Aldrich | Cat# SAB4200148; RRID: AB_10624068 |
| rabbit anti-Derlin-3 | Thermo Fisher Scientific | Cat# PA5-107110; RRID: AB_2817826 |
| mouse anti-Sec31A | BD Biosciences | Cat# 612351; RRID: AB_399717 |
| goat anti-mouse IgG2b AF647 | Cell Signaling Technologies | Cat# 57080 |
| Rabbit anti-GM130 | Abcam | Cat# Ab52649; RRID: AB_880266 |
| Goat anti-rabbit IgG AF647 | Abcam | Cat# Ab150091; RRID: AB_3719867 |
| **Bacterial and virus strains** | | |
| *E.coli* BL21-Gold(DE3) | Agilent | Cat# 200131 |
| $SPT^{WT}$ lentivirus | Cordes et al.[31] | N/A |
| $SPTC^{133W}$ lentivirus | Cordes et al.[31] | N/A |
| **Chemicals, peptides, and recombinant proteins** | | |
| *N*-phenyl-bis(trifluoromethanesulfonimide) | Sigma-Aldrich | Cat# 295973 |
| 1,4-dioxane | Sigma-Aldrich | Cat# 360481 |
| Triethylamine ($Et_3N$) | Sigma-Aldrich | Cat# 471283 |
| Lithium iodide (LiI) | Sigma-Aldrich | Cat# 8.18287 |
| *N*-Boc-ethylenediamine | Sigma-Aldrich | Cat# 15369 |
| palladium(II) acetate ($Pd(OAc)_2$) | Sigma-Aldrich | Cat# 8.18056 |
| cesium carbonate ($Cs_2CO_3$) | Sigma-Aldrich | Cat# 20959 |
| Bis(diphenylphosphino)-9,9-dimethylxanthene (Xantphos) | Sigma-Aldrich | Cat# 526460 |
| Trifluoroacetic acid (TFA) | Sigma-Aldrich | Cat# T6508 |
| O-(7-azabenzotriazol-1-yl)-1,1,3,3-tetramethyluronium hexafluorophosphate (HATU) | Sigma-Aldrich | Cat# 445460 |
| *N*,*N*-diisopropylethylamine (DIEA) | Sigma-Aldrich | Cat# D125806 |
| Formic acid | Sigma-Aldrich | Cat# F0507 |
| 2,7-Difluoro-6-hydroxy-9-(2-methylphenyl)-*3H*-xanthen-3-one (Pennsylvania Green) | AK Scientific, Inc. | Cat# AMTGC257 |
| Azidoacetic acid | TCI Chemicals | Cat# A3079 |
| Deuterated chloroform ($CDCl_3$) | Cambridge Isotope Laboratories | Cat# DLM-29-0 |
| 2S-amino-1,3R-octadecanediol (sphinganine d18:0) | Cayman Chemical | Cat# 10007945 |
| 2S-amino-3R-octadecanol (1-deoxysphinganine m18:0) | Cayman Chemical | Cat# 13511 |
| NBD-dodecanoic acid | Avantor Sciences | Cat# CDX-N0013 |
| Hydroxybenzotriazole (HOBt) | Sigma-Aldrich | Cat# 157260 |
| alkyne-sphinganine (alkyne-SA) | Vector Laboratories | Cat# CCT-1452 |
| alkyne-deoxysphinganine (alkyne-deoxySA) | Alecu et al.[24] | N/A |
| PennGreen-azide | This paper | N/A |
| AZDye488-picolyl azide | Vector Laboratories | Cat# CCT-1276 |

(*Continued on next page*)

*Continued*

| REAGENT or RESOURCE | SOURCE | IDENTIFIER |
|---|---|---|
| Fibronectin | Sigma-Aldrich | Cat# F1141 |
| Lipofectamine 3000 | Invitrogen | Cat# L3000 |
| Penicillin-streptomycin | Gibco | Cat# 15140122 |
| DMEM/F12 with L-glutamine | Gibco | Cat# 11320033 |
| Opti-MEM | Gibco | Cat# 31985070 |
| Dialyzed Fetal Bovine Serum | Gibco | Cat# 26400044 |
| MitoTracker Red FM | Thermo Fisher Scientific | Cat# M22425 |
| LysoTracker Deep Red | Thermo Fisher Scientific | Cat# L12492 |
| IPTG, dioxane-free 5G | Thermo Fisher Scientific | Cat# R0392 |
| Tris base | Fisher BioReagents | Cat# BP152-500 |
| Sodium chloride for molecular biology | Sigma-Aldrich | Cat# S3014 |
| OmniPure DTT | Sigma-Aldrich | Cat# 3860 |
| cOmplete® EDTA-free protease inhibitor cocktail | Roche | Cat# 11873580001 |
| Bestatin hydrochloride | Sigma-Aldrich | Cat# B8385 |
| Pepstatin A | Sigma-Aldrich | Cat# P5318 |
| Phosphoramidon disodium salt | Sigma-Aldrich | Cat# R7385 |
| DNAse I | Roche | Cat# 10104159001 |
| Glutathione reduced | Sigma-Aldrich | Cat# G4251 |
| InstantBlue | Abcam | Cat# ISB1L |
| Glycerol, 99+% Extra Pure | Thermo Fisher Scientific | Cat# 158920010 |
| HEPES | Fisher BioReagents | Cat# BP310-500 |
| 1,2-dioleoyl-sn-glycero-3-phosphatidylcholine (DOPC) | Avanti Polar Lipids | Cat# A80375 |
| 1,2-dipalmitoyl-sn-glycero-3-phosphoethanolamine-N-(lissamine rhodamine B sulfonyl) (Rhod-PE) | Avanti Polar Lipids | Cat# A81158 |
| NBD-dihydroceramide | This paper | N/A |
| NBD-deoxydihydroceramide | This paper | N/A |
| Recombinant CERT START domain | This paper | N/A |
| *N*-[(1R,3S)-3-hydroxy-1-(hydroxy methyl-3-phenylpropyl]-dodecanamide (HPA-12) | Sigma-Aldrich | Cat# SML2894 |
| 1-phenyl-2-decanoylamino-3-morpholino-1-propanol (PDMP) | Sigma-Aldrich | Cat# 513100 |
| Puromycin | Gibco | Cat# A1113803 |
| Doxycycline | Sigma-Aldrich | Cat# D9891 |
| Pierce™ RIPA buffer | Thermo Fisher Scientific | Cat# 89900 |
| 1X Halt protease inhibitor cocktail | Thermo Fisher Scientific | Cat# 78420 |
| Precision Plus Protein Dual Color standards | Bio-Rad | Cat# 1610374 |
| PVDF membrane | Bio-Rad | Cat# 1620174 |
| sphinganine-d7 | Avanti Polar Lipids | Cat# 860658 |
| deoxysphinganine-d3 | Avanti Polar Lipids | Cat# 860474 |
| d18:0-d7/13:0 dihydroceramide | Avanti Polar Lipids | Cat# 330726 |
| d18:1-d7/15:0 ceramide | Avanti Polar Lipids | Cat# 860681 |
| d18:1-d7/15:0 glucosylceramide | Avanti Polar Lipids | Cat# 330729 |
| d18:1-d7/15:0 lactosylceramide | Avanti Polar Lipids | Cat# 330727 |
| Sphingosine-d7 | Avanti Polar Lipids | Cat# 860657 |
| d18:1/18:1-d9 sphingomyelin | Avanti Polar Lipids | Cat# 791649 |
| Sphingomyelin (d18:1/18:1)-d9 | Avanti Polar Lipids | Cat# 860740 |
| Laurdan | Thermo Fisher Scientific | Cat# D250 |
| Biotin | Sigma-Aldrich | Cat# B4501 |

(*Continued on next page*)

*Continued*

| REAGENT or RESOURCE | SOURCE | IDENTIFIER |
|---|---|---|
| **Critical commercial assays** | | |
| Pierce™ BCA protein assay | Thermo Fisher Scientific | Cat# 23225 |
| SuperSignal West Pico Chemiluminescent Substrate | Thermo Fisher Scientific | Cat# 34580 |
| Seahorse Cell Mito Stress Test | Agilent | Cat# 103015 |
| **Experimental models: Cell lines** | | |
| hTERT-RPE-1 cells | ATCC | ID# CRL-4000 |
| RPE-1 $SPT^{WT}$ | This paper | N/A |
| RPE-1 $SPT^{C133W}$ | This paper | N/A |
| **Recombinant DNA** | | |
| mCherry-Sec23A | Weigel et al.[45] | Addgene #166894 |
| mCherry-Sec61β | J. Lippincott-Schwartz | N/A |
| mApple-Sec61β | J. Lippincott-Schwartz | N/A |
| Galactosyltransferase-mApple (GalT-mApple) | J. Lippincott-Schwartz | N/A |
| Sialyl Transferase-mApple (SiT-mApple) | J. Lippincott-Schwartz | N/A |
| pGEX-4-T1 | Genscript | Cat# V010918 |
| pGEX-4-T1 CERT START | This study | N/A |
| Str-KDEL_TfR-SBP-mCherry (TfR-mCherry) | Weigel et al.[45] | N/A |
| Str-KDEL_SBP-mApple-Ecadherin | J. Lippincott-Schwartz | N/A |
| Str-KDEL_TNF-SBP-mCherry (TNF-mCherry) | Boncompain et al.[59] | Addgene #65279 |
| Str-KDEL_SBP-mCherry-GPI (mCherry-GPI) | Boncompain et al.[59] | Addgene #65295 |
| Str-KDEL_SBP-mCherry-Gp135 (mCherry-Gp135-RUSH) | Weigel et al.[45] | N/A |
| **Software and algorithms** | | |
| ImageJ/Fiji version 2.0.0-rc-69/1.53o | National Institutes of Health | https://imagej.net/software/fiji/downloads |
| GraphPad Prism version 10.1.1 | GraphPad Software | https://www.graphpad.com/updates/prism-10-1-1-release-notes |
| ZEN Black version 2.3 | ZEISS | https://www.micro-shop.zeiss.com/en/us/softwarefinder/software-categories/zen-black/zen-black-system/ |
| Python 3.15 | Python Software Foundation | https://pypi.org/ |
| LaurdanSegmentation | This paper | Zenodo: https://doi.org/10.5281/zenodo.17874908 |
| **Other** | | |
| 35 mm glass bottom dishes No 1.5 Cover Slip | MatTek | Cat# P35G-1.5-14-C |
| Glutathione Sepharose™ 4B GST-tagged resin | Cytiva | Cat# 17075605 |
| Amicon Ultra 15 MWCO 10 kDa concentrator | Millipore | Cat# UFC9010 |
| Slide-A-Lyzer MWCO 3.5 kDa | Thermo Fisher Scientific | Cat# A52966 |
| mini-PROTEAN TGX gels | Bio-Rad | Cat# 4568026 |

## EXPERIMENTAL MODEL AND STUDY PARTICIPANT DETAILS

The parental line of the study, hTERT-RPE-1 (RPE-1), is near-diploid and female in origin. RPE-1 and derived lines ($SPT^{WT}$ and $SPT^{C133W}$) were cultured in DMEM/F12 medium with L-glutamine and 15mM HEPES, supplemented with 10% dialyzed fetal bovine serum and 1% penicillin-streptomycin. Cells were maintained in a 37°C humidified incubator kept in 5% $CO_2$ atmosphere. Cells were routinely tested for mycoplasma by Human Embryonic Stem Cell Core (Sanford Consortium). Cell lines were not validated after being

received by the supplier, but regular cell morphology, Golgi apparatus sturcutre, and monolayer formation capacity of RPE-1 was regularly checked.

## METHOD DETAILS

### Synthesis of new compounds

#### *General considerations for PennGreen-azide synthesis*

The reaction scheme for PennGreen-azide is shown in Figure S7A. Commercially available reagents obtained were obtained from suppliers in the key resources table and were used without further purification unless otherwise noted. Analytical thin-layer chromatography was performed on E. Merck silica gel 60 $F_{254}$ plates. Silica gel flash chromatography was performed using E. Merck silica gel (type 60SDS, 230-400 mesh). Solvent mixtures for chromatography are reported as v/v ratios. HPLC analysis was carried out on an Eclipse Plus C8 analytical column with *Phase A*/*Phase B* gradients [*Phase A*: $H_2O$ with 0.1% formic acid; *Phase B*: MeOH with 0.1% formic acid]. HPLC purification was carried out on Zorbax SB-C18 semipreparative column with *Phase A*/*Phase B* gradients [*Phase A*: $H_2O$ with 0.1% formic acid; *Phase B*: MeOH with 0.1% formic acid]. Proton nuclear magnetic resonance ($^1$H NMR) spectra were recorded on a Varian VX-500 MHz MHz spectrometer and were referenced relative to residual proton resonances in $CDCl_3$ (at $\delta$ 7.24 ppm). $^1$H NMR splitting patterns are assigned as singlet (s), doublet (d), triplet (t), quartet (q) or pentuplet (p). All first-order splitting patterns were designated on the basis of the appearance of the multiplet. Splitting patterns that could not be readily interpreted are designated as multiplet (m) or broad (br). Carbon nuclear magnetic resonance ($^{13}$C NMR) spectra were recorded on a Varian VX-500 MHz spectrometer and were referenced relative to residual proton resonances in $CDCl_3$ (at $\delta$ 77.23 ppm). Electrospray Ionization-Time of Flight (ESI-TOF) spectra were obtained on an Agilent 6230 Accurate-Mass TOFMS mass spectrometer.

#### *2,7-difluoro-6-iodo-9-(o-tolyl)-3H-xanthen-3-one (PennGreen iodide)*

To a dry, argon-flushed round-bottomed flask was added Pennsylvania Green[2,3] (PennGreen, 50.0 mg, 147.8 μmol) and *N*-phenyl-bis(trifluoromethanesulfonimide (63.4 mg, 177.4 μmol). Then, anhydrous 1,4-dioxane (1 mL) was added, followed by $Et_3N$ (24.7 μL, 177.4 μmol). The flask was heated under Ar to 60°C for 1 h [Note: Conversion to the intermediate triflate was observed by TLC and HPLC-MS]. The flask was removed from the oil bath and LiI (59.3 mg, 443.4 μmol) and a reflux condenser were added. The solution was refluxed (~110°C) for 4 h. The flask was cooled to rt. Then, aqueous 2M solution of NaOH (250 μL) was added, and the solution was stirred for 1 h. Afterwards, $H_2O$ (3 mL) was added, giving rise to a product slurry that was stirred for 1 h. After this time, the orange slurry was chilled to 4°C, filtered, and the product cake washed with cold $H_2O$ (3 × 1 mL) to give the product containing residual 1,4-dioxane. This product cake was treated with $Et_2O$ (250 μL), stirred vigorously for 1 min, and hexanes (250 μL) were added. The resulting slurry was filtered and the product cake extensively dried under high vacuum to provide 53.8 mg of PennGreen iodide as an orange solid [81%].$^1$H NMR ($CDCl_3$, 500.13 MHz, δ): 7.97 (d, $J_1$ = 5.1 Hz, $J_2$ = 0.8 Hz, 1H, 1 × CH), 7.52 (td, $J_1$ = 7.6 Hz, $J_2$ = 1.4 Hz, 1H, 1 × CH), 7.42 (ddd, $J_1$ = 16.4 Hz, $J_2$ = 7.9 Hz, $J_3$ = 1.4 Hz, 2H, 2 × CH), 7.14 (dd, $J_1$ = 7.6 Hz, $J_2$ = 1.4 Hz, 1H, 1 × CH), 6.70 (d, $J_2$ = 7.8 Hz, 1H, 1 × CH), 6.62 (dd, $J_1$ = 10.5 Hz, $J_2$ = 0.9 Hz, 1H, 1 × CH), 6.56 (dd, $J_1$ = 6.8 Hz, $J_2$ = 1.3 Hz, 1H, 1 × CH), 2.07 (s, 3H, 1 × $CH_3$). $^{13}$C NMR ($CDCl_3$, 125.77 MHz, δ): 176.9 (d, $J$ = 21.2 Hz), 159.4, 157.9, 157.4, 156.9, 155.8, 153.8, 148.1, 136.1, 131.4, 131.2, 130.4, 129.0, 128.0 (d, $J$ = 2.1 Hz), 126.8, 121.4 (dd, $J_1$ = 48.8 Hz, $J_2$ = 8.1 Hz), 111.1 (dd, $J_1$ = 267.8 Hz, $J_2$ = 25.0 Hz), 107.1 (d, $J$ = 4.6 Hz), 87.9 (d, $J$ = 29.2 Hz), 67.2,* 19.8. MS (ESI-TOF) [m/z (%)]: 448 ([MH]$^+$, 100).* NMR artifact (1,4-dioxane).

#### *2,7-difluoro-6-(N-Boc-ethylenediamine)-9-(o-tolyl)-3H-xanthen-3-one (N-Boc-EthD-PennGreen)*

An oven-dried microwave test tube was charged with PennGreen iodide (10.0 mg, 22.3 μmol), *N*-Boc-ethylenediamine (5.3 μL, 33.5 μmol), $Pd(OAc)_2$ (0.5 mg, 2.2 μmol), $Cs_2CO_3$ (14.5 mg, 44.6 μmol), and Xantphos (1.9 mg, 3.35 μmol). The test tube was slowly flushed with Ar. Then, anhydrous, degassed toluene (500 μL) was added. The test tube was sealed and heated to 120°C in a microwave reactor for 1 h. The reaction tube was cooled to rt and diluted with $CH_2Cl_2$ (2.5 mL). Then, $H_2O$ (1.5 mL) was added, and the organic layer was separated. The aqueous portion was extracted with $CH_2Cl_2$ (2 × 1.5 mL). The organic layers were combined, dried over anhydrous $Na_2SO_4$, and filtered. The solvent was removed under reduced pressure, giving an orange crude solid. The crude was purified by flash chromatography (0-5% MeOH in $CH_2Cl_2$), affording 6.1 mg of *N*-Boc-EthD-PennGreen as a red solid [57%, $R_f$ = 0.16 (2% MeOH in $CH_2Cl_2$)]. $^1$H NMR ($CDCl_3$, 500.13 MHz, δ): 7.48 (td, $J_1$ = 7.5 Hz, $J_2$ = 1.4 Hz, 1H, 1 × CH), 7.44-7.34 (m, 2H, 2 × CH), 7.13 (dd, $J_1$ = 7.6 Hz, $J_2$ = 1.4 Hz, 1H, 1 × CH), 6.80-6.53 (m, 4H, 4 × CH), 5.03-4.88 (m, 1H, 1 × NH), 4.11-3.99 (m, 1H, 1 × NH), 3.60-3.50 (m, 2H, 1 × $CH_2$), 3.49-3.39 (m, 2H, 1 × $CH_2$), 2.06 (s, 3H, 1 × $CH_3$), 1.45 (s, 9H, 3 × $CH_3$). $^{13}$C NMR ($CDCl_3$, 125.77 MHz, δ): 174.6, 157.6, 157.1, 154.8, 152.9, 152.0, 149.9, 148.0, 144.1, 136.0, 132.3, 131.0, 130.1, 128.9, 126.5, 115.2, 111.4 and 111.2, 110.6, 106.3, 96.8, 80.7, 39.5, 29.8, 28.4, 19.8. MS (ESI-TOF) [m/z (%)]: 481 ([MH]$^+$, 100).

#### *2,7-difluoro-6-(ethylenediamine)-9-(o-tolyl)-3H-xanthen-3-one ($H_2$N-EthD-PennGreen)*

A solution of *N*-Boc-EthD-PennGreen (3.0 mg, 6.3 μmol) in 200 μL of TFA/$CH_2Cl_2$ (1:1) was stirred at rt for 15 min. After removal of the solvent, the residue was dried under high vacuum for 3 h and used without further purification. MS (ESI-TOF) [m/z (%)]: 381 ([MH]$^+$, 100).

#### *2,7-difluoro-6-(azidoacetylethylenediamine)-9-(o-tolyl)-3H-xanthen-3-one ($N_3$-Ac-EthD-PennGreen; PennGreen-azide)*

A solution of azidoacetic acid (0.5 μL, 6.3 μmol) in 100 μL of $CH_2Cl_2$/DMF (1:1) was stirred at 0°C for 10 min, and then HATU (2.6 mg, 6.9 μmol) and DIEA (4.4 μL, 25.0 μmol) were successively added. After 10 min stirring at 0°C, a $H_2$N-EthD-PennGreen (2.4 mg, 6.3 μmol) solution in 100 μL of $CH_2Cl_2$/DMF (1:1) containing DIEA (2.2 μL, 12.5 μmol) was added. After 1 h stirring at rt, the solvent was removed under reduced pressure to give a red orange solid. The corresponding residue was dissolved in MeOH (200 μL), filtered using a 0.2 μm syringe-driven filter, and the crude solution was purified by HPLC, affording 2.4 mg of $N_3$-Ac-EthD-PennGreen

(PennGreen Azide) as an orange solid [84%, $t_R$ = 8.1 min (Zorbax SB-C18 semipreparative column, 50% *Phase A* in *Phase B*, 1 min, then 50-5% *Phase A* in *Phase B*, 5 min, and then 5% *Phase A* in *Phase B*, 7 min)]. $^1$H NMR ($CDCl_3$, 500.13 MHz, δ): 7.51 (td, $J_1$ = 7.7 Hz, $J_2$ = 1.4 Hz, 1H, 1 × CH), 7.41 (dd, $J_1$ = 16.0 Hz, $J_2$ = 7.8 Hz, 2H, 2 × CH), 7.35-7.28 (m, 1H, 1 × CH), 7.16-7.10 (m, 1H, 1 × CH), 7.07 (br s, 1H, 1 × NH), 6.92 (d, $J$ = 6.8 Hz, 1H, 1 × CH), 6.73 (dd, $J_1$ = 11.0 Hz, $J_2$ = 5.0 Hz, 2H, 2 × CH), 6.57 (br s, 1H, 1 × NH), 4.06 (s, 2H, 1 × $CH_2$), 3.84-3.65 (m, 2H, 1 × $CH_2$), 3.64-3.55 (m, 2H, 1 × $CH_2$), 2.04 (s, 3H, 1 × $CH_3$). $^{13}$C NMR ($CDCl_3$, 125.77 MHz, δ): 169.3, 166.0, 161.5, 156.6, 153.8, 150.3, 148.4, 135.9, 131.9, 131.1, 130.3, 130.2, 128.8, 128.0, 126.5, 115.1, 111.6 and 111.4, 111.2, 106.1, 97.0, 52.5, 44.9, 38.6, 19.8. MS (ESI-TOF) [m/z (%)]: 464 ([MH]$^+$, 100).

#### *General considerations for C12-NBD-DHCer and C12-NBD-deoxyDHCer synthesis*

The reaction scheme for C12-NBD compounds is shown in Figures S7B and S7C. Commercially available reagents obtained were obtained from suppliers in the key resources table and were used without further purification unless otherwise noted. HPLC analysis was carried out on a 1260 Infinity II LC System equipped with an Agilent C18 column, using Phase A/Phase B gradients (Phase A: $H_2O$ with 0.1% trifluoroacetic acid; Phase B: acetonitrile (ACN) with 0.1% trifluoroacetic acid). Proton nuclear magnetic resonance ($^1$H NMR) spectra were recorded on a 400 MHz Varian Mercury Plus spectrometer and referenced relative to residual proton resonances in $CDCl_3$ (δ 7.26 ppm). Carbon nuclear magnetic resonance ($^{13}$C NMR) spectra were recorded on the same instrument and referenced to $CDCl_3$ (δ 77.36 ppm). High-resolution mass spectrometry (HR-MS) measurements were obtained using an Agilent 1260 Infinity Binary LC instrument coupled to a 6230 Accurate-Mass TOFMS system.

#### *N-((2R)-1,3-dihydroxyoctadecan-2-yl)-12-((7-nitrobenzo[c][1,2,5]oxadiazol-4-yl)amino)dodecanamide (C12-NBD-DHCer)*

NBD-dodecanoic acid (3.8 mg, 10.1 μmol) was dissolved in 200 μL of DMF in a glass vial. HATU (4.8 mg, 12.6 μmol), DIEA (13.9 μL, 80.7 μmol), and HOBt (1.4 mg, 10.6 μmol) were added successively. The mixture was stirred under $N_2$ for 5 min at room temperature (RT), then a solution of 2S-amino-1,3R-octadecanediol (3.1 mg, 10.2 μmol) in 200 μL of DMF was added dropwise. The reaction mixture was stirred overnight at RT under $N_2$. After solvent removal in vacuo, an orange oil was obtained, which was dissolved in methanol, filtered through a 0.2 μm syringe-driven filter, and purified by HPLC. The product was isolated as a yellow oil (5.0 mg, 78% yield; $t_R$= 8.5 min; C18 semipreparative column; 50:50 Phase A:B for 2 min, ramp to 25:75 over 8 min, then to 1:99 over 4 min). $^1$H NMR ($CDCl_3$, 400 MHz, δ): 8.54 (d, J = 9.0 Hz, 1H, 1 × CH), 6.47 (d, J = 9.0 Hz, 1H, 1 × CH), 4.15 (m, 1H, 1 × CH), 4.02 (m, 1H, 1 × CH), 3.79 (m, 2H, 1 × $CH_2$), 3.49 (t, J = 4.0 Hz, 2H, 1 × $CH_2$), 2.26 (t, J = 7.6 Hz, 2H, 1 × $CH_2$), 1.81–1.64 (m, 4H, 2 × $CH_2$), 1.34–1.21 (br m, 32H, 16 × $CH_2$), 0.88 (t, J = 7.0 Hz, 3H, 1 × $CH_3$). $^{13}$C NMR ($CDCl_3$, 101 MHz, δ): 144.1, 134.2, 124.2, 77.1 (solvent), 61.0, 39.0, 36.0, 33.7, 32.0, 30.0, 29.8, 29.6, 29.5, 29.4, 27.2, 26.1, 22.8, 14.2. HR-ESI-TOFMS: *m/z* [M + Na]$^+$ calcd for $C_{36}H_{63}N_5O_6Na$ = 684.4671; found = 684.4670.

#### *N-((2R)-3-hydroxyoctadecan-2-yl)-12-((7-nitrobenzo[c][1,2,5]oxadiazol-4-yl)amino)dodecanamide (C12-NBD-deoxyDHCer)*

NBD-dodecanoic acid (3.8 mg, 10.1 μmol) was dissolved in 200 μL of DMF in a glass vial. HATU (4.8 mg, 12.6 μmol), DIEA (13.9 μL, 80.7 μmol), and HOBt (1.4 mg, 10.6 μmol) were added successively. The mixture was stirred under $N_2$ for 5 min at RT, then a solution of 2S-amino-3R-octadecanol (2.9 mg, 10.2 μmol) in 200 μL of DMF was added dropwise. The reaction mixture was stirred overnight at RT under $N_2$. After solvent removal in vacuo, a yellow oil was obtained, which was dissolved in methanol, filtered through a 0.2 μm syringe-driven filter, and purified by HPLC. The product was isolated as a orange oil (6.1 mg, 91% yield; $t_R$ = 8.6 min; Agilent C18 semipreparative column; 50:50 Phase A:B for 2 min, ramp to 25:75 over 8 min, then to 1:99 over 4 min). $^1$H NMR ($CDCl_3$, 400 MHz, δ): 8.54 (d, 1H, 1 × CH), 6.19 (m, 1H, 1 × CH), 4.02 (m, 2H, 1 × $CH_2$), 3.65 (m, J = 6.4 Hz, 1H, 1 × CH), 3.49 (d, J = 6.4 Hz, 2H, 1 × $CH_2$), 2.21 (t, J = 7.6 Hz, 2H, 1 × $CH_2$), 1.89–1.60 (m, 6H, 3 × $CH_2$), 1.45–1.20 (br m, 28H, 14 × $CH_2$), 0.87 (t, J = 6.8 Hz, 3H, 1 × $CH_3$). $^{13}$C NMR ($CDCl_3$, 101 MHz, δ): 144.1, 136.4, 134.6, 73.97, 50.7, 33.3, 31.8, 29.5, 29.5, 29.5, 29.4, 29.4, 29.4, 29.3, 29.2, 29.1, 29.1, 29.0, 29.0, 28.9, 28.9, 28.3, 26.7, 25.8, 25.6, 22.5, 14.0. HR-ESI-TOFMS: *m/z* [M + Na]$^+$ calcd for $C_{36}H_{63}N_5O_5Na$ = 668.4721; found = 668.4727.

### Cell line generation and analysis

#### *Transient transfection*

For microscopy-based assays, cells were first seeded into 35 mm glass bottom dishes #1.5 coverslip MatTek dishes coated with 2 μg fibronectin/cm$^2$. For transient expression of proteins, cells were transfected with Lipofectamine 3000 in Opti-MEM media for 5 h and changed into complete growth medium. Cells were imaged 24 h after transfection or later depending on the treatment.

#### *Generation of new cell lines*

Stable cell lines expressing SPTLC-1$^{WT}$ (SPT$^{WT}$) and SPTLC-1$^{C133W}$ (SPT$^{C133W}$) were generated using lentiviral transduction as previously described.[31] In brief, 6 μL or lentivirus particles harboring each ORF were added to RPE-1 in 0.5 mL medium containing 6 μg/mL polybrene for 4 h before addition of 2 mL virus-free growth medium. After 24 h, the medium was changed to standard growth medium containing 5 μg/mL puromycin for 10 days, refreshing every 48 h. After puromycin selection, immunoblotting was carried out to confirm the expression of SPTLC-1 in response to doxycycline.

#### *Physiological assays*

For analysis of cell line growth, RPE-1, SPT$^{WT}$ and SPT$^{C133W}$ lines were seeded in 96-well plates with starting density of 500 cells/well. Each cell line was seeded in 20 wells; in 10 of these wells, cells were treated with 1 μg/ml of doxycycline at time of seeding, and the other 10 wells were left untreated. Cell growth was performed by live cell imaging with a Incucyte Sx5 automated confluency imager

(Satorius). Images were acquired every hour for 6 days and analyzed to determine cell confluency relative to the initial state at 0 hours.

For analysis of respiration in stable cell lines expressing $SPT^{WT}$ and $SPT^{C133W}$, 20,000 cells were seeded in biological replicates (N=3) into 96 well Seahorse cell culture microplates pretreated with fibronectin. Upon attachment, cells were induced with 1 μg/mL doxycycline for 48h prior to analysis on the Agilent Seahorse XF pro (Agilent Technologies). Subsequently, samples were analyzed using the Seahorse Cell Mito Stress Test with sequential addition of 1.5 μM oligomycin, 1 μM carbonyl cyanide-p-trifluoromethoxy phenylhydrazone (FCCP) and 0.5 μM of Rotenone/Antimycin A mixture. After the assay, cells were trypsinized and mixed with trypan blue to count the live cells for normalization of respiration rates.

## Imaging

### *Bioorthogonal labeling*

The alkyne-sphinganine (alkyne-SA) and alkyne-deoxysphinganine (alkyne-deoxySA) probes were previously described.[24] For Cu(I)-catalyzed azide-alkyne cycloadditions (CuAAC), cells were fed with 0.1 μM of either alkyne-SA or alkyne-deoxySA for 17 hr, after which cells were rinsed with PBS and fixed with cold 4% paraformaldehyde and 0.1% glutaraldehyde in PBS for 20 min. Fixed cells were quenched with 100 mM glycine in PBS, washed twice, and CuAAC was performed by adding a mixture of 5 μM PennGreen-azide or 10 μM AZDye488 picolyl-azide, 100 μM $CuSO_4$, 500 μM BTTAA and 1 mM ascorbic acid in PBS. Cells were allowed to react for 45 min in the dark at room temperature, followed by 3 washes with PBS. Hoescht staining was performed afterwards at a 1:5,000 dilution for 5 min. For the picolyl-azide experiments, 6 wash steps were carried out with 15 min incubations each, and then a final overnight wash step in PBS was performed before imaging. This was required to completely wash out unreacted dye. For colocalization experiments with ERES (Figure 4), cells were transfected with mCherry-Sec23. To verify the localization of PennGreen-azide probe (Figure S1A), cells were transfected with mCherry-Sec61β (ER) or SiT-mApple (Golgi) or stained with either MitoTracker Red FM or LysoTracker Deep Red. To quantify the fluorescent intensity of each PennGreen or AZDye488 labeled cell, integrated intensity was measured across a region of interest (ROI) corresponding to the cell periphery. The CTCF value was then generated by subtracting the background signal from an area equivalent to ROI from that integrated intensity.

### *Confocal microscopy*

All cells were grown and transfected on MatTek dishes with #1.5 coverslip. Confocal microscopy was performed on a Zeiss LSM 880 microscope equipped with plan-apochromat 64x/1.4 NA or 20x/0.8 NA objectives. For Pennsylvania Green and AZDye488 experiments, cells were excited with a 488 nm Argon laser at 0.5% power. For mCherry, and mApple experiments, a 561 nm diode laser was used. For AF647 immunofluorescence experiments, a 633 nm HeNe laser was used at 1-2% power. All images used for intensity quantification were acquired in LSM mode. Airyscan imaging was performed using Plan Apo 63x/1.4 objective on ZEISS LSM 880 with Airyscan. Live-cell confocal experiments were conducted with cells incubated at 37°C with 5% $CO_2$ and humidified air. For GP measurements, Laurdan dye was excited with 405 nm diode laser set at 0.3% power and emission was detected using QUASAR GaAsP detector set to two simultaneous spectrum windows: 436±18 for ordered membrane emission and 498±18 for disordered membrane emission.

### *Membrane fluidity analysis*

For Laurdan experiments, cells were seeded and either induced with 1 μg/mL doxycycline for 48 hours ($SPT^{WT}$ and $SPT^{C133W}$ cell lines) or treated with different inhibitors, prior to the staining protocol. Upon completion of treatment, cells were washed with HBSS and stained with 5 μM Laurdan dye for 30 min in serum-free DMEM/F12 media. Staining solution was then replaced with complete growth media before imaging. To calculate GP values of specific secretory membranes, cells were also transfected with different organelle markers, mCherry-Sec61β for ER and SiT-mApple for Golgi apparatus or stained with CellMask Deep Red for plasma membrane.

To quantify the GP value of specific secretory membranes, cell images were acquired in 3 different spectral channels. A binary mask was first created with the image of a particular organelle marker to define the region of interest (ROI) and the resulting mask was then applied to images acquired on the ordered channel (436±18 nm) and disordered channel (498±18 nm). The GP was calculated at each pixel as described previously[52] by utilizing the following equation:

$$GP = \frac{I_{ordered} - G I_{disordered}}{I_{ordered} + G I_{disordered}}$$

In this equation, *I* represents the intensity of each pixel in the image obtained from the specified spectral channel. The G factor compensates for experimental variations and ensures that GP measurements are comparable across different experiments. The G factor was calculated as previously described[52] using diluted dye in pure DMSO. Visual heatmaps were generated with Python's seaborn library to show the spatial distribution of GP values across the organelle.

### *ERES analysis*

In mCherry-Sec23 transfected cells, Individual endoplasmic reticulum exit sites (ERES) were cropped from the original image. From each cell, 10-20 well-separated exit sites were manually cropped; the sample type was blinded during this process. For each condition, 6-12 cells were chosen for this. The length of each square pixel was defined from the dimensions of the image given by ImageJ with the used microscope setting. To define the number of pixels comprising each ERES, the region of interest was automatically segmented. For this, Otsu's threshold was used to calculate an appropriate threshold value for the image. The area of each ERES was then measured by converting from the number of pixels to square microns.

For immunofluorescence of SEC31, cells were induced for 48 hours, washed with PBS, and fixed with 4% paraformaldehyde and 0.1% glutaraldehyde in cold PBS for 10 min. Fixed cells were quenched with 100 mM glycine in PBS for 15 min, washed twice, and then incubated in blocking buffer (3% BSA 0.01% saponin in PBS) overnight at 4°C. Cells were then washed 4 times and incubated with a mouse anti-SSEC31A antibody overnight at 4°C. After 4 washes, cells were incubated with goat anti-mouse IgG2b AF647 for 1 hour, washed and washed an additional 3 times.

#### *Synchronized cargo release*

For live-cell experiments, cells were transiently transfected with single-lent RUSH systems containing both hook and cargo. Cargoes were released upon addition of 40 μM of biotin on the microscope stage. Time series were acquired with 5 or 10 min intervals. Signal associated with the Golgi region was analyzed after acquisition by integrating signal intensity in a hand-drawn region corresponding to the apparent Golgi region observed during the time-series. For this, Fiji was used alongside the StackReg plugin. This integrated intensity was normalized to the total cargo intensity across the cell.

For fixed-cell experiments, cells were fixed at discrete time points with cold 4% paraformaldehyde and 4% sucrose for 20 min at room temperature in the dark. Fixed cells were then washed with PBS followed by permeabilization and blocking in 0.05% saponin and 1% BSA in PBS. Permeabilized cells were then incubated with an anti-GM130 primary antibody (1:500 dilution) in the same buffer at 4°C overnight. After three washes, the samples were incubated with a AF647-labeled secondary antibody (1:500 dilution) for 1 hour. The stained samples were washed three times and imaged at room temperature. To quantify the fraction of cargo in the Golgi compartment at a given time point, images of the Golgi marker (GM130) and the fluorescent cargo were segmented using Otsu's method. The fraction of fluorescent cargo signal present in the Golgi was then calculated by dividing the sum of fluorescent cargo pixel intensities overlapping with the Golgi marker by the total fluorescent cargo pixel intensity.

### Biochemistry

#### *Purification of CERT START domain*

The START domain of CERT ($START_{CERT}$) was synthesized and cloned into a pGEX-4-T1 vector (Genescript) for expression in fusion at the C-terminus of a GST domain followed by a thrombin cleavage site. $START_{CERT}$ was expressed in *E.coli* BL21-Gold(DE3) for 16 h in LB-Lennox supplemented with 0.5 mM IPTG after the optical density (OD) at 600 nm reached 0.9. Pellets were obtained after a first centrifugation of the culture (30 min, 3500 g, 4°C), and second centrifugation (30 min, 3500 g, 4°C) after resuspension in cold PBS (1:10 initial culture volume). The pellet was frozen at -20°C until subsequent protein extraction and purification. All purification steps were performed in cold and degassed TN buffer (50 mM Tris-base, 300 mM NaCl, pH 8.0 at 4°C adjusted with HCL). From 1 L of culture, frozen bacterial pellets were resuspended in 100 mL TN buffer supplemented with 1 mM DTT (TND buffer), 2 tablets of Complete® EDTA-free protease inhibitor cocktail (Roche), 10 μM bestatin, 1 μg/mL pepstatin A, and 10 μM phosphoramidon. Cells were lysed by passing them twice through a homogenizer, EmulsiFlex-C3 (Avestin), the lysate was then doped with 200 mM PMSF, then 5 mM MgCl2 and 20 μg/mL DNAse I and clarified by ultracentrifugation (186,000 g, 1h, 6°C), soluble protein containing supernatant was applied to Glutathione Sepharose slurry (3% v/v) and incubated 3.5 hr at 4°C. The resin was then packed and washed 4 times with 10 volumes of TND buffer using an Econo-Pac chromatography column. Bound proteins were eluted with TND buffer supplemented with 10 mM glutathione reduced. The eluate was collected and purity determined by SDS-PAGE. GST-CERT containing fractions were diluted to 15 mL with TN buffer and concentrated to 2 mL twice using an ultrafiltration device (MWCO 10 kDa). The protein was further purified by size exclusion chromatography on an Akta Pure 25 FPLC with a Sephacryl S200 HR column equilibrated with TN buffer at a flow rate of 1 mL/min and fractionation volume of 2.5 mL. Samples were concentrated, supplemented with 10% glycerol (v/v), flash frozen in liquid $N_2$ and stored at -80°C until further use. Sample purity was confirmed by mass identification on an Agilent 6230 time-of-flight mass spectrometer (TOFMS) with JetStream electrospray ionization source ESI (LC-ESI-TOFMS) after dialysis (MWCO 3.5 kDa) in low salt TN buffer (10 mM Tris-HCl, 50 mM NaCl, pH 7.4).

#### *Lipid transfer activity of CERT*

DOPC (1,2-dioleoyl-sn-glycero-3-phosphocholine), and Rhod-PE (1,2-dipalmitoyl-sn-glycero-3-phosphoethanolamine-N-(lissamine rhodamine B sulfonyl)), which were used from stock solutions in $CHCl_3$. The concentrations of NBD-dihydroceramide (N-[(E,2S,3R)-1,3-dihydroxyoctadec-4-en-2-yl]-12-[(4-nitro-2,1,3-benzoxadiazol-7-yl)amino]dodecanamide and NBD-deoxydihydroceramide (N-[(2S,3R,4E)-3-hydroxyoctadec-4-en-2-yl]-12-[(7-nitro-2,1,3-benzoxadiazol-4-yl)amino]dodecanamide) in methanol were determined by absorbance at 463 nm ($\varepsilon$ = 22,000 $M^{-1}cm^{-1}$). Liposomes were prepared as previously described.[92] Briefly, desired molar ratios of lipids were combined from stock solutions in a pear-shaped flask and dried under vacuum using a rotary evaporator with a water bath set at 40°C. The resulting lipid films were resuspended in preheated HK buffer (40°C; 50 mM HEPES, 120 mM potassium acetate, pH 7.4, adjusted with KOH) using four sterile glass beads and vigorous vortexing for 5 min to ensure complete resuspension of the waxy lipids. Vesicle lamellarity was then reduced by five freeze–thaw cycles. Large unilamellar vesicles (LUVs) were subsequently obtained by extrusion through a 0.2 μm perforated polycarbonate membrane using a mini-extruder and syringes pre-heated to 60°C. The NBD-ceramide transfer from liposome donor ($L_A$) to liposomes acceptor ($L_B$) was measured by recording the dequenching of NBD fluorescence on Cary Eclipse Fluorescence Spectrophotometer (Agilent). In a 500 μL rectangular quartz suprasil cuvette (Perkin Elmer), stirred with a magnetic bar, 200 μM of $L_A$ liposome were added (186 μM DOPC, 10 μM C12-NBD-DHCer or C12-NBD-deoxyDHCer, 4 μM Rhodamine PE). The NBD fluorophore was recorded at 538 nm (excitation slit = 5 nm) under excitation at 473 nm (slit = 2.5 nm) with a photomultiplier set to 800 V, and measurement interval of 0.5 sec. At t = 1 min, 200 μM of $L_B$ liposomes (200 μM DOPC) were added to the cuvette, a slow (~0.23 nM / min) spontaneous transfer is measured over two min. CERT was then added at a final concentration of 200 nM and the kinetics of transfer was recorded over 12 min. For inhibition, CERT protein samples

were incubated with five molar excess of HPA-12 in DMSO (10 mM stock) or with 0.036% DMSO and incubated at room temperature for 5 min before measuring the activity. To determine the amount of lipid transported, the maximal fluorescence (Fmax) under equilibrium condition was measured by mixing 200 μM $L_{A\text{-}eq}$ liposomes (191 μM DOPC, 5 μM C12-NBD-DHCer or C12-NBD-deoxyDHCer, 4 μM Rhodamine PE) and 200 μM $L_{B\text{-}eq}$ liposomes (195 μM DOPC, 5 μM C12-NBD-DHCer or C12-NBD-deoxyDHCer, 4 μM Rhodamine PE). The concentration of NBD-lipid transported was calculated from the recorded fluorescence signal (F) using the following equation: [Conc] = (F - $F_0$) / ($F_{max}$ - F0) * 5 ; where $F_0$ represents the average fluorescence over 6 seconds prior CERT injection in each independent measurement, and $F_{max}$ corresponded to the average fluorescence over 5 min under equilibrium conditions after 9 min incubation, from three independent experiments. The initial rate was determined from the slope of a linear regression over the 4 first seconds following protein injection.

### *Western blotting*

To confirm the integration of *SPTLC1*$^{WT}$ and *SPTLC1*$^{C133W}$ alleles into hTERT-RPE-1 cell line under titratable *tet* promoter, puromycin selected cells were plated on T-25 flasks in growth medium containing 10% dialyzed FBS and doxycycline. After 48 h of induction with doxycycline at different concentrations, cells were washed twice with cold PBS and lysed in ice-cold Pierce™ RIPA buffer supplemented with 1X Halt protease inhibitor cocktail and incubated for 5 min at 4°C. Cell lysates were then collected and centrifuged at 14,000 g for 15 min at 4°C. Supernatants were used to quantify protein concentration using Pierce™ BCA protein assay kit. Samples were incubated for 5 min at 95°C in 1X Laemmli buffer. 12 μg of total protein was separated on a 4-20% SDS-PAGE gel along with Precision Plus Protein Dual Color standards (Bio-Rad), and proteins were transferred onto a 0.2 μm PVDF membrane. The membrane was blocked with 5% nonfat milk in TBS buffer with 0.1% Tween-20 (TBST) for 1 hour at room temperature and immunoblotted with primary antibody at 4°C overnight diluted in 5% nonfat milk, anti-SPTLC1 (1:500 dilution), and anti-β-actin (1:1,000 dilution). The immunoblots were then washed 3 times with TBST and incubated with secondary antibody for 3 hours at room temperature (1:2,000 dilution, anti-rabbit HRP conjugate for SPTLC1; 1:2,000 dilution, anti-mouse HRP conjugate for β-actin). Specific signal was detected using SuperSignal West Pico Chemiluminescent Substrate and imaged with a ChemiDoc XRS+ (Bio-Rad) imaging station.

For analysis of ER stress response, SPT$^{WT}$ and SPT$^{C133W}$, cell lines were seeded in 6-well plates with a starting seeding density of 200,000 cells/well. Cells were induced with 1 μg/ml of doxycycline after 24 hours. Cells were harvested 48 hours post-induction. Protein levels were detected using the following primary antibodies: rabbit anti-IRE1-phosphorylated (1:1,000), rabbit anti-AKT-phosphorylated (1:1,000), mouse anti-Derlin-1 (1:2,000), rabbit anti-Derlin-3 (1:2,000).

### Lipid mass spectrometry

Cells were spiked with the following internal standards: 20 pmol sphinganine-d7, deoxysphinganine-d3, 100 pmol d18:0-d7/13:0 dihydroceramide, 200 pmol d18:1-d7/15:0 ceramide, 100 pmol d18:1-d7/15:0 glucosylceramide, 100 pmol d18:1-d7/15:0 lactosylceramide, 200 pmol sphingosine-d7, and 200 pmol d18:1/18:1-d9 sphingomyelin or 200 pmol sphingomyelin (d18:1/18:1)-d9. Cells were scraped in a solution containing 0.5 mL methanol and 0.5 mL water. A 100 μL aliquot of the homogenate was set aside to determine protein concentration using a BCA protein assay. The remaining homogenate was transferred to a new Eppendorf tube, followed by the addition of 1 mL of chloroform. The samples were vortexed for 5 min and centrifuged at 15,000 g for 5 min at 4°C. The organic phase was collected, and 2 μL of formic acid was added to the polar phase, which was re-extracted with an additional 1 mL of chloroform. The organic phases were combined and dried under nitrogen.

Sphingolipids were quantified using an Agilent 6460 QQQ LC-MS/MS system. Separation was achieved on a C8 column (Spectra 3 μm C8SR 150 × 3 mm). Dried extracts were resuspended in 100 μL of Buffer B (methanol with 1 mM ammonium formate and 0.2% formic acid), sonicated for 10 min, centrifuged at 15,000g for 10 min at 4°C, and 80 μL of the supernatant was transferred into vials for analysis. A 5 μL injection was made into the system. The mobile phase consisted of HPLC-grade water (phase A) with 2 mM ammonium formate and 0.2% formic acid, and methanol (phase B) with 1 mM ammonium formate and 0.2% formic acid. The flow rate was set at 0.5 mL/min and the gradient elution program was as follow: 82% B from 0 to 4 min, raised to 90% B over 14 min, raised to 99% B over 7 min, kept at 99% B for 2 min, and decreased to 82% B over 3 min, for a total run time of 30 min. A post-run of 10 min followed each sample allowing for the column re-equilibration. Sphingolipid species were detected using multiple reaction monitoring (MRM) of the transition from precursor to product ions[93] with optimized collision energies and fragmentor voltages. Specific MRMs for sphinganine (SA), sphingosine (SO), and sphingosine-1-phosphate (S1P) were recorded from 0 to 10 min, while MRMs for dihydroceramide (DHCer), ceramide (Cer), hexosyl-ceramide (HexosylCer), lactosyl-ceramide (LactosylCer), and sphingomyelin (SM) were recorded from 10 to 30 min. Relative sphingolipid abundances were calculated by normalizing abundances to internal standards specific to their respective class and to protein content.

## QUANTIFICATION AND STATISTICAL ANALYSIS

Replication details, including number of cells, independent samples/dishes, and number of subcellular structures, are provided in the legend of each figure legend or in the STAR Methods section. For significance, data were statistically analyzed using GraphPad Prism 10.1.1 (GraphPad Software). Specific statistical tests were chosen according to the experiment design and specified in the corresponding figure legend where the significance level is indicated. All image quantification was performed using Python and ImageJ. The following Python packages were used in thresholding and intensity computation: numpy, pandas, skimage, seaborn, matplotlib and os. Specific thresholds were applied to binarize the image in Python, essentially creating a mask for the fluorescent region of interest.